

# Ly $\alpha$ emission in low-redshift most metal-deficient compact star-forming galaxies

Y. I. Izotov<sup>1</sup>, T. X. Thuan<sup>2</sup>, N. G. Guseva<sup>1</sup>, D. Schaerer<sup>3,4</sup>, G. Worseck<sup>5</sup>,  
A. Verhamme<sup>3</sup>

<sup>1</sup>*Bogolyubov Institute for Theoretical Physics, National Academy of Sciences of Ukraine, 14-b Metrolohichna str., Kyiv, 03143, Ukraine, E-mail: yizotov@bitp.kiev.ua, nguseva@bitp.kiev.ua*

<sup>2</sup>*Astronomy Department, University of Virginia, P.O. Box 400325, Charlottesville, VA 22904-4325, USA, E-mail: txt@virginia.edu*

<sup>3</sup>*Observatoire de Genève, Université de Genève, 51 Ch. des Maillettes, 1290, Versoix, Switzerland, E-mail: daniel.schaerer@unige.ch, anne.verhamme@unige.ch*

<sup>4</sup>*IRAP/CNRS, 14, Av. E. Belin, 31400 Toulouse, France*

<sup>5</sup>*Institut für Physik und Astronomie, Universität Potsdam, Karl-Liebknecht-Str. 24/25, D-14476 Potsdam, Germany, E-mail: gworseck@web.de*

Accepted XXX. Received YYY; in original form ZZZ

## ABSTRACT

We present observations with the Cosmic Origins Spectrograph onboard the *Hubble Space Telescope* of nine most metal-deficient compact star-forming galaxies with oxygen abundances  $12 + \log(\text{O}/\text{H}) = 6.97 - 7.23$ , redshifts  $z = 0.02811 - 0.13320$ , and stellar masses  $M_{\star} \leq 10^7 M_{\odot}$ . We aim to study the properties of Ly $\alpha$  emission in these extremely metal-deficient objects. We find that all nine galaxies are Ly $\alpha$  emitters (LAEs). We examine various relations between the Ly $\alpha$  escape fraction  $f_{\text{esc}}(\text{Ly}\alpha)$  and other characteristics – such as absolute UV magnitude, oxygen abundance, O<sub>32</sub> ratio, stellar mass, Lyman-alpha luminosity and equivalent width EW(Ly $\alpha$ ), ionizing photon production efficiency  $\xi_{\text{ion}}$  and velocity separation  $V_{\text{sep}}$  between the two peaks of the Ly $\alpha$  profile – of a large sample of LAEs, including our lowest-metallicity galaxies and other objects from the literature. We find a relatively tight correlation between  $f_{\text{esc}}(\text{Ly}\alpha)$  and two characteristics, EW(Ly $\alpha$ ) and  $V_{\text{sep}}$ , whereas no correlation is found between  $f_{\text{esc}}(\text{Ly}\alpha)$  and the oxygen abundance. We also find a relatively tight relation between the Ly $\alpha$  and LyC escape fractions. We propose to use the latter relation to estimate indirectly the escaping ionizing radiation in LAEs, when direct measurements of LyC emission are not possible. We show that the global properties of low- $z$  LAEs are very similar to those of  $z > 6$  galaxies. They are thus ideal local proxies for studying physical processes during the epoch of reionization of the Universe.

**Key words:** (cosmology:) dark ages, reionization, first stars — galaxies: abundances — galaxies: dwarf — galaxies: fundamental parameters — galaxies: ISM — galaxies: starburst

## 1 INTRODUCTION

Theoretical and observational studies over the last decade have suggested that the agents responsible for the reionization of the Universe, which ends at  $z \sim 6$ , are likely to come from a dominant population of low-mass and very metal-poor dwarf galaxies (Ouchi et al. 2009; Wise & Chen 2009; Kashikawa et al. 2011; Jiang et al. 2013; Mitra, Ferrara & Choudhury 2013; Yajima, Choi & Nagamine 2011; Bouwens et al. 2015; Smith et al. 2018; Naidu et al. 2018; Steidel et al. 2018; Kimm et al. 2019). On the observational side, recent work including some of the first observations of the *James Webb Space Telescope* (JWST) revealed large popu-

lations of UV-faint galaxies at  $z > 6$  with low stellar masses ( $M_{\star} \sim 10^6 - 10^8 M_{\odot}$ ), active star formation with specific star-formation rates sSFR of  $\sim 100 \text{ Gyr}^{-1}$ , and likely extremely low metallicities, although the latter are to be confirmed by further observations (e.g. Pentericci et al. 2018; Fuller et al. 2020; Kikuchihara et al. 2020; Schaerer et al. 2022; Curti et al. 2023; Ning et al. 2023; Endsley et al. 2023a,b; Saxena et al. 2023; Macsía et al. 2023; Matthee et al. 2023; Simmonds et al. 2023; Santini et al. 2023; Trump et al. 2023; Chen et al. 2023; Rhoads et al. 2022; Fujimoto et al. 2023; Lin et al. 2023; Atek et al. 2023). These galaxies are characterized by high ionizing photon production effi-

ciencies  $\xi_{\text{ion}}$  of  $\sim 10^{25.5} - 10^{25.8}$  Hz erg $^{-1}$ , and are likely numerous enough to be able to reionize the Universe. Many of these galaxies show strong Lyman-alpha emission, and so are classified as Lyman-alpha emitters (LAEs) (e.g. Jones et al. 2023; Saxena et al. 2023; Tang et al. 2023; Jung et al. 2023; Ning et al. 2023).

However, despite these recent advances, those dwarf star-forming galaxies (SFGs) at high redshifts are very faint and most of them still escape detection or do not allow detailed studies by modern large telescopes. Therefore, it is important to search for local counterparts of these high-redshift dwarf SFGs to study their properties in detail.

In particular, the profiles of the resolved Ly $\alpha$  emission line are used as indirect indicators of escaping LyC emission. These profiles in the spectra of most of low- $z$  LyC leakers and LAEs are double-peaked, with the peak separation  $V_{\text{sep}}$  increasing with increasing optical depth in the Ly $\alpha$  emission line, which depends on the neutral hydrogen column density  $N(\text{H I})$  (e.g. Izotov et al. 2016a,b, 2018a,b). Only in a few galaxies, the Ly $\alpha$  profile consists of more peaks (Rivera-Thorsen et al. 2017; Izotov et al. 2018b; Vanzella et al. 2018).

The relation between the LyC escape fraction  $f_{\text{esc}}(\text{LyC})$  and the Ly $\alpha$  peak separation is tight (Verhamme et al. 2015; Izotov et al. 2018b), making  $V_{\text{sep}}$  the reliable indicator of escaping LyC emission. Furthermore, Verhamme et al. (2017) have shown that the Ly $\alpha$  escape fractions  $f_{\text{esc}}(\text{Ly}\alpha)$  are larger than the LyC escape fractions  $f_{\text{esc}}(\text{LyC})$ , in accord with theoretical predictions of Dijkstra, Gronke & Venkatesan (2016) and simulations of Maji et al. (2022). A more detailed analysis of simulated Lyman-alpha profiles is given in Blaizot et al. (2023). Izotov et al. (2020) found that the Ly $\alpha$  escape fraction also anticorrelates with  $V_{\text{sep}}$ , but not as tightly as  $f_{\text{esc}}(\text{LyC})$ .

Very low-metallicity galaxies are much fainter than the LyC leaking galaxies studied before at  $z \sim 0.3 - 0.4$ . In fact, no galaxy with  $12+\log(\text{O}/\text{H}) \lesssim 7.25$  is known in the Sloan Digital Sky Survey (SDSS) at these redshifts. Only at very low redshifts,  $z \lesssim 0.1$ , are the extremely low-metallicity galaxies sufficiently bright to be selected for spectroscopic observations in the SDSS. Since these XMDs have low redshifts, direct observations of the Lyman continuum are not possible with the *HST*/COS. Therefore, our intention is to use the Ly $\alpha$  profiles in their spectra to derive information about possible leaking LyC radiation in galaxies that have much lower stellar masses and metallicities than confirmed LyC leakers.

The primary objective of this paper is to obtain for the first time UV spectra with the Ly $\alpha$  line of nine low-redshift ( $z \lesssim 0.13$ ) compact, extremely metal-deficient (XMD) SFGs, with  $12+\log\text{O}/\text{H} = 6.97 - 7.23$ . Such galaxies are extremely rare in the local Universe, but they likely were common at the epoch of reionization (e.g. Langan, Severino & Finlator 2020). The proposed XMD sample is the most complete one known so far, including all objects gathered from the latest Data Release 16 (DR16) of the SDSS, that satisfy the selection criteria described below. This sample includes the two SFGs with the lowest  $12+\log(\text{O}/\text{H})$  known until now, J0811+4730 and J1234+3901 ( $12+\log(\text{O}/\text{H})=6.98, 7.03$ , Izotov et al. 2018c, 2019). To date, only one *HST*/COS spectrum has been obtained for a SFG in that extreme metallicity range, but with much less extreme conditions in

its H II regions, that of I Zw 18 (James et al. 2014). The UV spectrum of I Zw 18 shows a broad Ly $\alpha$  absorption line, without any sign of Ly $\alpha$  emission.

The proposed observations will considerably increase the sample of XMDs observed in the Ly $\alpha$  line range, and extend the range of  $12+\log(\text{O}/\text{H})$  down to  $\text{O}/\text{H} \sim 1/50$  of the solar value, as derived by Asplund et al. (2009). Because of their very low metallicities, low stellar masses and extremely high star-formation activity, these XMDs are likely the closest local analogues of the primordial dwarf galaxies in the early Universe. Strong Ly $\alpha$  in emission has been seen in most low- $z$  LyC leakers with higher metallicity by Izotov et al. (2016a,b, 2018a,b, 2021a, 2022) and Flury et al. (2022). The galaxies studied here have lower metallicities and stellar masses than previously observed Ly $\alpha$  emitting galaxies such as the galaxies at  $z < 0.07$  with extreme  $\text{O}_{32}$  ratios of  $> 20$  (Izotov et al. 2020), the “green pea” (GP) galaxies with  $z \sim 0.1 - 0.3$  studied e.g. by Jaskot et al. (2017), Yang et al. (2017), McKinney et al. (2019), and the confirmed LyC leakers at  $z \sim 0.3 - 0.4$  (Izotov et al. 2016a,b, 2018a,b).

We examine here whether the lowest-metallicity galaxies also possess strong Ly $\alpha$  emission. Such objects will be called hereafter “extreme Ly $\alpha$  emitters” or “xLAEs”. The observations probe a new metallicity domain with *HST*, and the spectra provide important insight on a variety of topics/questions concerning these galaxies, including their Ly $\alpha$  and LyC escape, their ISM and radiation field.

The selection criteria are presented in Section 2. The properties of the selected galaxies derived from SDSS observations in the optical range, and from UV and mid-infrared observations with the *GALEX* and *WISE* space telescopes, respectively, are discussed in Section 3. The *HST* observations and data reduction are described in Section 4. The surface brightness profiles in the UV range are discussed in Section 5. Ly $\alpha$  emission is considered in Section 6. In Section 7, we compare the Ly $\alpha$  escape fractions obtained for our galaxies in this paper and for other galaxies in some recent studies. Our results are summarized in Section 8.

## 2 SELECTION CRITERIA

We use the SDSS Data Release 16 (DR16) (Ahumada et al. 2020) to select galaxies, applying the following criteria:

- the temperature-sensitive [O III]  $\lambda 4363$  emission line in the SDSS spectrum is detected at the level greater than  $3\sigma$  to allow accurate abundance determination;
- the oxygen abundance of the ionized gas in the H II region, derived using the direct  $T_e$ -method, is  $12+\log(\text{O}/\text{H}) < 7.25$ ;
- the redshift  $z$  of the galaxy is greater than 0.02, to avoid contamination from the wings of the Milky Way Ly $\alpha$  absorption line;
- no bright objects must be present in vicinity of the galaxy to satisfy COS safety requirements;
- the galaxy is sufficiently compact in the SDSS image for detection of the total galaxy flux inside the 2.5 arcsec (in diameter) COS spectroscopic aperture;
- the galaxy should be isolated inside the 2.5 arcsec COS spectroscopic aperture to avoid contamination from other sources;
- the *GALEX* NUV magnitude of the galaxy is brighter

**Table 1.** Some general characteristics of the selected galaxies from the SDSS data base

Name	R.A.(2000.0)	Dec.(2000.0)	$z$	$D_L^a$ (Mpc)	$D_A^b$ (Mpc)	$O_{32}^c$	EW(H $\beta$ ) ( $\text{\AA}$ )	FWHM <sup>d</sup> (arcsec)	12+log(O/H) <sup>e</sup>
J0122+0048	01:22:41.62	+00:48:42.06	0.05734	258	231	4.8	156	1.52	7.22
J0139+1542	01:39:11.93	+15:42:41.32	0.02811	124	117	5.9	339	1.19	7.22
J0811+4730	08:11:52.12	+47:30:26.24	0.04442	198	181	9.6	331	1.21	6.97
J0837+1921	08:37:21.87	+19:21:10.63	0.06734	305	268	10.7	134	1.03	7.21
J1004+3256	10:04:09.90	+32:56:12.51	0.06639	301	264	37.0	459	1.61	7.16
J1206+5007	12:06:08.53	+50:07:21.17	0.05129	230	208	5.6	219	1.67	7.15
J1234+3901	12:34:15.70	+39:01:16.41	0.13320	630	491	14.1	276	1.28	7.03
J1505+3721	15:05:08.58	+37:21:40.22	0.07532	343	297	15.8	298	1.40	7.23
J2229+2725	22:29:33.19	+27:25:25.60	0.07622	347	300	54.8	580	0.93	7.11

<sup>a</sup>Luminosity distance (NED, Wright 2006).

<sup>b</sup>Angular size distance (NED, Wright 2006).

<sup>c</sup> $O_{32} = [\text{O III}]\lambda 5007/[\text{O II}]\lambda 3727$ .

<sup>d</sup>Full width at half maximum in the SDSS  $g$ -band image.

<sup>e</sup>Oxygen abundance derived by the  $T_e$ -method from line intensities in the SDSS spectrum.

**Table 2.** Apparent magnitudes with errors in parentheses compiled from the SDSS, GALEX and WISE data bases

Name	SDSS (AB)					GALEX (AB)		WISE (Vega)			
	$u$ (err)	$g$ (err)	$r$ (err)	$i$ (err)	$z$ (err)	FUV (err)	NUV (err)	W1 (err)	W2 (err)	W3 (err)	W4 (err)
J0122+0048	22.02 (0.17)	21.62 (0.06)	22.18 (0.13)	21.75 (0.14)	22.19 (0.60)	21.90 (0.34)	21.52 (0.27)	...	...	...	...
J0139+1542	22.24 (0.29)	21.84 (0.07)	22.12 (0.13)	22.39 (0.25)	21.89 (0.57)	23.88 (0.28)	22.17 (0.15)	...	...	...	...
J0811+4730	22.30 (0.28)	21.38 (0.05)	22.17 (0.17)	21.56 (0.12)	23.05 (0.70)	...	22.79 (1.06)	...	...	...	...
J0837+1921	22.10 (0.14)	21.91 (0.05)	22.87 (0.17)	21.99 (0.13)	21.84 (0.38)	21.25 (0.33)	21.53 (0.49)	...	...	...	...
J1004+3256	22.13 (0.23)	21.33 (0.05)	22.13 (0.16)	20.98 (0.09)	22.24 (0.81)	...	22.35 (0.18)	...	...	...	...
J1206+5007	22.21 (0.29)	21.76 (0.07)	22.42 (0.20)	22.24 (0.25)	21.42 (0.47)	22.28 (0.14)	22.25 (0.12)	17.13 (0.09)	17.10 (0.30)	...	...
J1234+3901	21.97 (0.14)	21.92 (0.06)	21.93 (0.09)	21.47 (0.09)	22.24 (0.54)	21.37 (0.08)	21.40 (0.07)	...	...	...	...
J1505+3721	21.20 (0.11)	20.97 (0.03)	21.69 (0.08)	20.60 (0.04)	21.79 (0.48)	21.54 (0.32)	21.29 (0.18)	...	...	...	...
J2229+2725	21.96 (0.15)	21.47 (0.04)	22.27 (0.11)	20.97 (0.05)	21.43 (0.33)	21.45 (0.28)	21.88 (0.37)	...	...	...	...

than  $\sim 22.5$  mag to be acquired with COS and to obtain spectra of reasonably good quality.

These selection criteria gave a total sample of nine galaxies.

### 3 INTEGRATED PROPERTIES OF SAMPLE GALAXIES

The SDSS spectra of the selected galaxies reveal extremely low oxygen abundances, in the range  $12 + \log(\text{O}/\text{H}) = 6.97 - 7.23$  (Tables 1, A2). These are considerably lower as compared to the oxygen abundances of the low-redshift Ly $\alpha$  and LyC leakers observed so far.

The sample galaxies show very high rest-frame equivalent widths  $\text{EW}(\text{H}\beta) = 156 - 580 \text{ \AA}$  (Table 1), indicating very recent star formation. All galaxies are characterised by high  $O_{32}$  ratios ranging from  $\sim 5$  to the very extreme value of  $\sim 55$ . Both high values of  $\text{EW}(\text{H}\beta)$  and  $O_{32}$  are conse-

quences of the selection criterion requiring the detection of the  $[\text{O III}] \lambda 4363$  emission line with sufficient accuracy (Table A1). This line is strongest in the youngest bursts of star formation.

All selected galaxies are faint in the optical range, with the SDSS  $g$  magnitude fainter than  $\sim 21$  mag (Table 2). However, despite their faintness in the optical range, all galaxies were detected by *Galaxy Evolution Explorer* (GALEX) in the NUV range and most of them were detected in the FUV range, because of a strongly rising continuum from the optical to the UV range. On the other hand, only one galaxy was detected in the mid-infrared range by the *Wide-field Infrared Survey Explorer* (WISE) (Table 2), indicating that emission from the red stellar population and dust is very weak.

The interstellar extinction is obtained from the hydrogen Balmer decrement in the SDSS spectra. We derive the ionized gas metallicity from the same spectra using the pre-

**Table 3.** Integrated characteristics

Name	$M_{\text{FUV}}^{\text{SED a}}$	$M_{\text{FUV}}^{\text{b}}$	$M_g^{\text{c}}$	$\log M_\star^{\text{d}}$	$\log L(\text{H}\beta)^{\text{e}}$	SFR <sup>f</sup>	sSFR <sup>g</sup>	$\log \xi_{\text{ion}}^{\text{h}}$	$\alpha^{\text{i}}$	$r_{50}^{\text{j}}$	$\Sigma_1^{\text{k}}$	$\Sigma_2^{\text{l}}$
J0122+0048	-16.15	-15.16	-15.44	7.00	40.02	0.23, 0.05	23	25.45	0.12	0.030	5.1	81
J0139+1542	-14.43	-11.59	-13.63	5.15	39.47	0.06, 0.02	425	25.54	0.04	0.013	11.9	113
J0811+4730	-15.21	...	-15.10	5.88	39.94	0.19, 0.06	250	25.71	...	...	...	...
J0837+1921	-16.12	-16.17	-15.51	6.24	40.10	0.28, 0.08	161	25.53	0.14	0.023	4.5	169
J1004+3256	-16.42	...	-16.09	6.24	40.31	0.45, 0.13	259	25.67	0.14	0.030	7.3	159
J1206+5007	-15.52	-14.53	-15.05	6.26	39.82	0.15, 0.05	82	25.46	0.13	0.030	2.8	53
J1234+3901	-18.03	-17.61	-17.08	6.94	40.85	1.57, 0.56	180	25.74	0.21	0.050	11.3	200
J1505+3721	-16.71	-16.14	-16.71	6.48	40.70	1.11, 0.29	368	25.69	0.19	0.045	9.8	175
J2229+2725	-16.43	-16.25	-16.23	6.39	40.49	0.68, 0.08	640	25.81	0.20	0.040	12.5	313

<sup>a</sup> $M_{\text{FUV}}^{\text{SED}}$  is the absolute FUV magnitude derived from the intrinsic rest-frame SED.

<sup>b</sup> $M_{\text{FUV}}$  is the absolute FUV magnitude derived from the apparent *GALEX* magnitude.

<sup>c</sup> $M_g$  is the absolute SDSS *g* magnitude corrected for the Milky Way extinction.

<sup>d</sup> $M_\star$  is the stellar mass in solar masses.

<sup>e</sup> $L(\text{H}\beta)$  is the extinction-corrected  $\text{H}\beta$  luminosity in  $\text{erg s}^{-1}$ .

<sup>f</sup>SFR is the star-formation rate in  $\text{M}_\odot \text{yr}^{-1}$ . The first value is derived from the extinction-corrected  $\text{H}\beta$  luminosity whereas the second value is determined from the extinction-corrected UV luminosity at  $\lambda = 1500\text{\AA}$ .

<sup>g</sup>Specific star formation rate  $\text{sSFR} = \text{SFR}/M_\star$  in  $\text{Gyr}^{-1}$ , where SFR is derived from the  $\text{H}\beta$  luminosity.

<sup>h</sup> $\xi_{\text{ion}}$  is the ionizing photon production efficiency in  $\text{Hz erg}^{-1}$  defined as  $\xi_{\text{ion}} = N_{\text{LyC}}/L_\nu$ , where  $N_{\text{LyC}}$  is the Lyman continuum photon production rate derived from the extinction-corrected  $\text{H}\beta$  luminosity and  $L_\nu$  is the monochromatic luminosity at  $\lambda = 1500\text{\AA}$  derived from the intrinsic rest-frame SED.

<sup>i</sup> $\alpha$  is the exponential disc scale length in kpc.

<sup>j</sup> $r_{50}$  is the galaxy radius in kpc where the NUV intensity is equal to half of the maximal intensity.

<sup>k</sup> $\Sigma_1$  is the star-formation rate surface density in  $\text{M}_\odot \text{yr}^{-1} \text{kpc}^{-2}$ , assuming the galaxy radius to be equal to  $\alpha$ .

<sup>l</sup> $\Sigma_2$  is the star-formation rate surface density in  $\text{M}_\odot \text{yr}^{-1} \text{kpc}^{-2}$ , assuming the galaxy radius to be equal to  $r_{50}$ .

scriptions of [Izotov, Thuan & Lipovetsky \(1994\)](#) and [Izotov et al. \(2006\)](#).

The emission-line fluxes corrected for extinction, adopting the [Cardelli, Clayton & Mathis \(1989\)](#) reddening law with  $R(V) = 2.7$ , the extinction coefficients  $C(\text{H}\beta)$ , the rest-frame equivalent widths of the  $\text{H}\beta$ ,  $[\text{O III}]\lambda 5007$  and  $\text{H}\alpha$  emission lines, and the observed  $\text{H}\beta$  fluxes are shown in Table A1. The fluxes from Table A1 and the direct  $T_e$  method are used to derive the electron temperatures, the electron number densities and the element abundances in the  $\text{H II}$  regions. These quantities are shown in Table A2.

However, we note that oxygen abundances derived from the SDSS spectra can sometime be incorrect because strong emission lines such as  $[\text{O III}]\lambda 4959$ , 5007 can be clipped, resulting in overestimated electron temperatures and, thus underestimated oxygen abundances. Therefore, additional observations with other telescopes are needed to check the very low metallicities of the selected galaxies. We have used the LBT to obtain spectrophotometric observations for the three galaxies with the lowest metallicities in our sample, J0811+4730 ([Izotov et al. 2018c](#)), J1234+3901 ([Izotov, Thuan & Guseva 2019](#)), and J2229+2725 ([Izotov, Thuan & Guseva 2021c](#)). The SDSS abundances are in good agreement with the LBT ones for these three galaxies.

The emission-line luminosities and stellar masses of our galaxies were obtained adopting a luminosity distance (NASA Extragalactic Database (NED), [Wright 2006](#)), with the cosmological parameters  $H_0 = 67.1 \text{ km s}^{-1} \text{Mpc}^{-1}$ ,  $\Omega_\Lambda = 0.682$ ,  $\Omega_m = 0.318$  ([Ade et al. 2014](#)). We also derived absolute magnitudes  $M_g$  and  $M_{\text{FUV}}$  in the SDSS *g* and *GALEX* FUV bands (Table 3), assuming negligible dust extinction.

The  $\text{H}\beta$  luminosities  $L(\text{H}\beta)$  and corresponding star-formation rates  $\text{SFR}(\text{H}\beta)$  shown in Table 3 were obtained from the extinction-corrected  $\text{H}\beta$  fluxes, using the relation

by [Kennicutt \(1998\)](#) and adopting the extinction-corrected  $\text{H}\alpha/\text{H}\beta$  flux ratios. They are more than one order of magnitude lower than the respective values for LyC leakers ([Izotov et al. 2016a,b, 2018a,b, 2021a, 2022](#)). Specific star formation rates  $\text{sSFR}(\text{H}\beta) = \text{SFR}(\text{H}\beta)/M_\star$  are  $\sim 100 \text{ Gyr}^{-1}$ , similar to  $\text{sSFR}(\text{H}\beta)$  for LyC leakers ([Izotov et al. 2016a,b, 2018a,b, 2021a](#)) and are several orders of magnitude higher than the sSFRs of the SDSS main sequence SFGs. We also use the extinction-corrected monochromatic UV luminosity at the rest-frame wavelength of  $1500\text{\AA}$  and equation 2 from [Madau, Pozzetti & Dickinson \(1998\)](#) to derive  $\text{SFR}(\text{UV})$ . We find it to be several times lower than  $\text{SFR}(\text{H}\beta)$  (Table 3). A similar difference between  $\text{SFR}(\text{H}\beta)$  and  $\text{SFR}(\text{UV})$  has also been found by other authors, for example by [Atek et al. \(2023\)](#) for a sample of low-mass and low-metallicity SFGs at  $z \sim 6 - 8$ . This likely is typical for low-mass galaxies with bursts of star formation as the relations by [Kennicutt \(1998\)](#) and [Madau, Pozzetti & Dickinson \(1998\)](#) are obtained by assuming long periods of star formation of  $\sim 100 \text{ Myr}$  and  $1 \text{ Gyr}$ , respectively, which may not be applicable for our xLAEs. However, we show these quantities for the sake of comparison because they are commonly used in many studies of bursting SFGs.

We use the extinction-corrected SDSS spectra of xLAEs to derive the stellar and nebular spectral energy distributions (SED), stellar masses, starburst ages and the modelled intrinsic absolute magnitudes  $M_{\text{FUV}}^{\text{SED}}$  in the FUV range. The star-formation history is approximated by a single instantaneous burst with an age  $< 10 \text{ Myr}$  and a continuous star formation with a constant star-formation rate and an age  $> 10 \text{ Myr}$ . All parameters such as stellar mass, starburst age and time interval for continuous star formation are derived iteratively by minimizing differences between the continua of the modelled SED and SDSS spectra. The SED fitting method, using a two-component stellar+nebular model, is

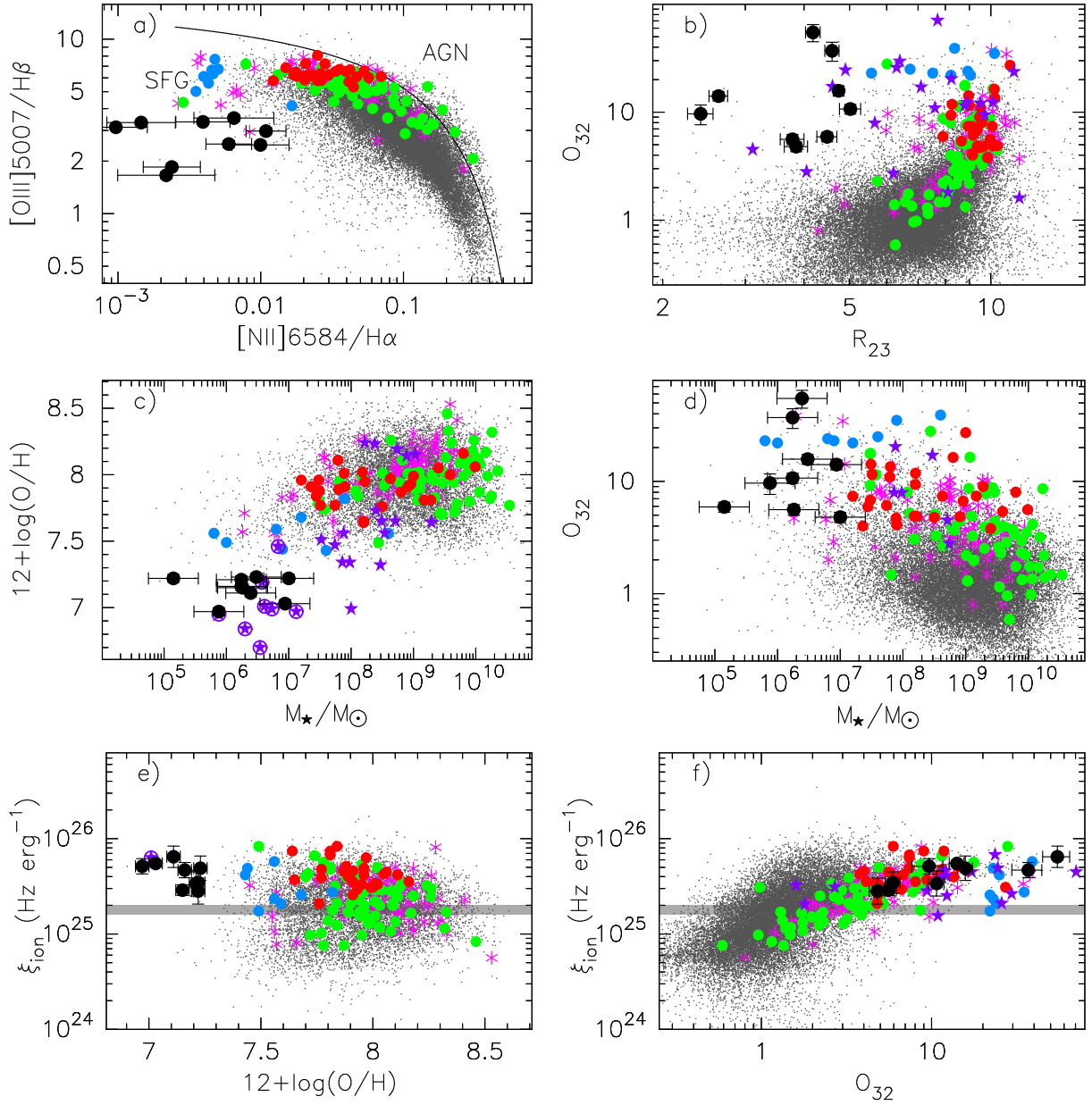


**Figure 1.** a) The Baldwin-Phillips-Terlevich (BPT) diagram (Baldwin et al. 1981) for SFGs. b) The  $O_{32} - R_{23}$  diagram for SFGs where  $R_{23} = ([O\text{ II}]\lambda 3727 + [O\text{ III}]\lambda 4959 + [O\text{ III}]\lambda 5007)/H\beta$ . c) and d) Dependencies of the oxygen abundances  $12+\log(O/H)$  and  $O_{32}$  ratios, respectively, on the stellar masses  $M_*$ . e) and f) Dependencies of the ionizing photon efficiencies  $\xi_{\text{ion}}$  on the oxygen abundances  $12+\log(O/H)$  and  $O_{32}$  ratios, respectively. In all panels, the xLAEs (this paper) with the respective errors are shown by black filled circles, the low-redshift ( $z < 0.1$ ) LAEs with high  $O_{32}$  (Izotov et al. 2020) are represented by blue filled circles, LyC leaking galaxies by Izotov et al. (2016a,b, 2018a,b, 2021a, 2022) are shown by red filled circles, the LyC galaxies by Flury et al. (2022) are shown by green filled circles and low- $z$  LAEs by Henry et al. (2015), Jaskot & Oey (2014), Jaskot et al. (2017), Yang et al. (2016, 2017), Xu et al. (2022), Hu et al. (2023) are represented by magenta asterisks. The references on the high- $z$  ( $z > 6$ ) LAEs (purple stars) are given in Table 4. Separately, by encircled purple stars, are shown  $z \sim 6 - 7$  XMDs in c) and their  $\xi_{\text{ion}}$  and  $12+\log(O/H)$  average values in e) (Atek et al. 2023). The compact SFGs from the SDSS (Izotov et al. 2021b) are represented by grey dots. The solid line in a) by Kauffmann et al. (2003) separates SFGs from active galactic nuclei (AGN). Values of  $\xi_{\text{ion}}$  assumed in canonical Universe reionisation models are shown in e) and f) with a horizontal grey shaded region (e.g. Robertson et al. 2013; Bouwens et al. 2016).

described e.g. in Izotov et al. (2018a). We find that the stellar masses and FUV luminosities of our galaxies are  $\sim 2$  orders of magnitude lower than those of the confirmed LyC leakers (Table 3). Their extinction-corrected absolute FUV magnitudes are in general considerably fainter than those of the faintest galaxies at  $z = 6 - 8$  observed thus far with the

JWST (e.g. Jones et al. 2023; Matthee et al. 2023; Saxena et al. 2023; Shapley et al. 2023).

In Fig. 1 we compare the integrated properties of our selected galaxies with various samples of low- $z$  LyC leaking galaxies and LAEs published by Izotov et al. (2016a,b, 2018a,b, 2020, 2021a, 2022), Flury et al. (2022), Jaskot &

**Table 4.** References on data for  $z \gtrsim 6$  galaxies

Figure	Relation	References
Fig. 1b	$O_{32}-R_{23}$	Saxena et al. (2023) Heintz et al. (2022)
Fig. 1c	$12+\log(O/H)-M_*/M_\odot$	Langeroodi et al. (2022) Jones et al. (2020) Heintz et al. (2022) Atek et al. (2023)
Fig. 1d	$O_{32}-M_*/M_\odot$	Heintz et al. (2022)
Fig. 1e	$\log \xi_{\text{ion}}-12+\log(O/H)$	Atek et al. (2023)
Fig. 1f	$\log \xi_{\text{ion}}-O_{32}$	Saxena et al. (2023)
Fig. 6a	$L(\text{Ly}\alpha)-M_{\text{FUV}}$	Jung et al. (2022) Ning et al. (2023) Fuller et al. (2020)
Fig. 6b	$\text{EW}(\text{Ly}\alpha)-M_{\text{FUV}}$	Jung et al. (2022) Ning et al. (2023) Jones et al. (2020) Fuller et al. (2020) Saxena et al. (2023)
Fig. 7a	$f_{\text{esc}}(\text{Ly}\alpha)-M_{\text{FUV}}$	Pentericci et al. (2018) Saxena et al. (2023) Ning et al. (2023)
Fig. 7c	$f_{\text{esc}}(\text{Ly}\alpha)-O_{32}$	Saxena et al. (2023)
Fig. 7e	$f_{\text{esc}}(\text{Ly}\alpha)-L(\text{Ly}\alpha)$	Simmonds et al. (2023) Ning et al. (2023)
Fig. 7f	$f_{\text{esc}}(\text{Ly}\alpha)-\log \xi_{\text{ion}}$	Saxena et al. (2023) Ning et al. (2023) Simmonds et al. (2023)
Fig. 7g	$f_{\text{esc}}(\text{Ly}\alpha)-\text{EW}(\text{Ly}\alpha)$	Saxena et al. (2023) Ning et al. (2023)

Oey (2014), Henry et al. (2015), Jaskot et al. (2017), Yang et al. (2016, 2017), Hu et al. (2023), as well as with the high- $z$  LAEs observed at  $z \gtrsim 6$ , during the period of the reionization. References for high- $z$  galaxies are given in Table 4. The errors are not available for some galaxies in the comparison sample. Therefore, the error bars in this Figure and all others are shown only for the galaxies in our sample (black symbols).

In the Baldwin-Phillips-Terlevich (BPT) diagnostic diagram (Fig. 1a), our sample galaxies (black filled circles) strongly deviate from the SFG branch (grey dots), from low-redshift Ly $\alpha$  emitters with  $O_{32} \gtrsim 20$ , but with higher metallicities (blue filled circles), from  $z \sim 0.3 - 0.4$  LyC leakers (red and green filled circles) and from other LAEs (magenta asterisks). These deviations result from their extremely low metallicities. In this sense, our xLAEs are considerably more extreme than other LAEs observed thus far with the *HST*/COS.

In the same vein, it can be seen in Fig. 1b, which shows the  $O_{32} - R_{23}$  diagram, that the xLAEs are also the most deviating objects from the SDSS main SFG sequence (grey dots), again because of their extremely low metallicities. On the other hand, most of the confirmed LyC leakers with higher metallicities (red and green filled circles) and other low- $z$  LAEs (magenta asterisks) are mainly located on the main sequence defined by SFGs. However, we note that high- $z$  ( $z \gtrsim 6$ ) LAEs (purple stars in the Figure) are also systematically offset from the main sequence, with the most deviating being the  $z \sim 8 - 9$  galaxies of Heintz et al. (2022), indicating their extremely low metallicities.

**Table 5.** *HST*/COS observations

Name	Date	Exposure time (s)	
		MIRRORA	G130M (Central wavelength) ( $\text{\AA}$ )
J0122+0048	2022-09-16	$2 \times 400$	6889 (1222)
J0139+1542	2022-11-14	$2 \times 600$	9337 (1222)
J0811+4730	2023-03-25	$2 \times 0$	5658 (1222)
J0837+1921	2023-03-20	$2 \times 500$	9537 (1222)
J1004+3256	2023-01-20	$2 \times 600$	9433 (1222)
J1206+5007	2023-03-09	$2 \times 600$	10045 (1222)
J1234+3901	2022-11-16	$2 \times 600$	9526 (1291)
J1505+3721	2023-02-22	$2 \times 400$	7058 (1291)
J2229+2725	2022-09-20	$2 \times 500$	9586 (1291)

Our xLAEs follow the mass-metallicity relation (Fig. 1c), having until recently both lower metallicities and masses than low- $z$  LyC leakers and high- $z$  LAEs (compare the locations of the black circles with those of the red and green circles and purple stars in Fig. 1c). But Atek et al. (2023) have recently discussed a sample of  $z \sim 6 - 8$  XMDs with stellar masses and oxygen abundances similar to those of the xLAEs. These galaxies are represented by encircled purple stars in Fig. 1c). We note, however, that only the H $\beta$  and [O III]  $\lambda 4959, 5007$  emission lines were detected in most of these galaxies, whereas only upper limits were obtained for the [O II]  $\lambda 3727$  emission line intensities. Therefore, the oxygen abundance is derived from the [O III]  $\lambda 5007/\text{H}\beta$  flux ratio, which depends not only on the oxygen abundance, but also on the ionization parameter. Therefore, the oxygen abundances derived by Atek et al. (2023) are somewhat uncertain. We also note that no data on Ly $\alpha$  emission are presented.

Our xLAEs also have on average higher  $O_{32}$  ratios compared e.g. to those of low- $z$  LyC leakers and high- $z$  LAEs (compare the locations of the black circles with those of the red, green and purple symbols in Fig. 1d).

Finally, all xLAEs have very high ionizing photon production efficiencies  $\xi_{\text{ion}}$  (Fig. 1e). Their values compare well with those for the high- $z$  XMDs of Atek et al. (2023), low- $z$  LAEs with high  $O_{32}$  ratios of  $> 20$  (Izotov et al. 2020), and for low- $z$  LyC leaking galaxies from the Izotov et al. (2016a,b, 2018a,b, 2021a, 2022) sample. This is because all have high EW(H $\beta$ ) and thus young starburst ages. The  $\xi_{\text{ion}}$  values of our xLAEs are well above the canonical values (horizontal lines) usually used in the Universe reionization models (Bouwens et al. 2016). For comparison, LyC leaking galaxies from the Flury et al. (2022) sample (green filled circles) and low- $z$  LAEs (magenta asterisks) have lower  $\xi_{\text{ion}}$ s, which compare well with the canonical value and those of the SDSS main sequence star-forming galaxies. We also note that there is no dependence of  $\xi_{\text{ion}}$  on the oxygen abundance

12+log(O/H) (Fig. 1e), whereas there is a clear dependence of  $\xi_{\text{ion}}$  on the O<sub>32</sub> ratio (Fig. 1f). This is a consequence of the direct dependence of O<sub>32</sub> on the ionization parameter.

#### 4 HST/COS OBSERVATIONS AND DATA REDUCTION

HST/COS observations of the nine most metal-deficient galaxies were obtained during the period September 2022 – March 2023 in program GO 16672 (PI: Y. I. Izotov), (Table 5). The galaxies were acquired by COS near-ultraviolet (NUV) imaging. The brightest region in the image of each target was centered in the 2.5 arcsec diameter spectroscopic aperture (Fig. 2). Unfortunately, acquisition observations for the most metal-deficient galaxy in our sample, also the most metal-deficient SFG known to-date, J0811+4730, failed. Therefore, the imaging data for this galaxy are not present. The spectroscopic observations of J0811+4730 were also affected by technical problems, so only part of the scheduled time was used. However, the quality of the J0811+4730 spectrum was sufficiently high so that we decided not to request a repeat observation.

The other eight galaxies show a very compact structure (Fig. 2), superposed on a low-surface-brightness (LSB) component. Most of the NUV continuum in these galaxies is concentrated in central regions with full widths at half maximum  $\lesssim$  0.1 arcsec, which is much smaller than the central unvignetted 0.8 arcsec diameter region of the spectroscopic aperture.

Spectra with Ly $\alpha$  emission lines were obtained with the COS G130M grating, positioned at the central wavelength of 1222 Å for six galaxies, and at 1291 Å for three galaxies with higher redshifts (J1234+3901, J1505+3721 and J2229+2725) because the resolving power of the 1222 Å setup declines at wavelengths longer than  $\sim$  1250 Å. The grating was positioned at the COS Detector Lifetime Position 4, yielding a spectral resolving power  $\lambda/\Delta\lambda \simeq$  14,000 in the wavelength range of interest. Spectra with the grating centered at 1222 Å were obtained in Segments A and B, covering a wavelength range of  $\sim$  300 Å, whereas spectra with the grating centered at 1291 Å were obtained only in Segment A, giving a wavelength coverage of  $\sim$  150 Å. No observation with Segment B is allowed for the latter configuration. All four focal-plane offset positions were employed to correct for grid wire shadows and detector blemishes. For two galaxies, J1505+3721 and J2229+2725, the blue components of Ly $\alpha$  emission are partly contaminated by emission from the geocoronal O I  $\lambda$ 1304 line. In those cases, a special requirement was made to observe those galaxies only during the periods with maximal shadow time intervals, when the brightness of the geocoronal line is minimal. Fortunately, the effect of contamination was not high, allowing to obtain the profiles of the Ly $\alpha$  blue components in both galaxies.

The spectra were reduced with the CALCOS pipeline v3.3.4, followed by accurate background subtraction and co-addition of individual exposures with custom software (Makan et al. 2021). These reduction procedures are analogous to those used by Izotov et al. (2016a,b, 2018a,b, 2020, 2021a, 2022).

#### 5 SURFACE BRIGHTNESS DISTRIBUTION IN THE NUV RANGE

Using the COS acquisition images, we obtain the surface brightness (SB) profiles of xLAEs in the NUV range with a linear decrease (in magnitudes) in the outer part and a sharp increase in the central part because of the presence of the bright star-forming region(s) (Fig. 3). The shape of the SB profiles in these galaxies is similar to those of confirmed LyC leakers (Izotov et al. 2016a,b, 2018a,b, 2021a, 2022), but with the considerably smaller scale lengths  $\alpha$  of our galaxies, in the range  $\leq$  0.21 kpc (Fig. 3, Table 3), compared to  $\alpha =$  0.6 – 1.8 kpc in LyC leakers (Izotov et al. 2016a,b, 2018a,b, 2021a, 2022). These scale lengths are similar to the smallest  $\alpha$  found for low- and high- $z$  compact star-forming galaxies (Papaderos et al. 2002; Izotov et al. 2020; Macsía et al. 2023). On the other hand, the surface densities of star-formation rate  $\Sigma = \text{SFR}(\text{H}\beta)/(\pi\alpha^2)$  in the studied galaxies are comparable to those of LyC leakers. The half-light radii  $r_{50}$  of our galaxies in the NUV are considerably smaller than  $\alpha$  because of the compactness of the bright star-forming regions (see Table 3). Therefore, the corresponding surface densities of star-formation rate  $\Sigma = \text{SFR}(\text{H}\beta)/(\pi r_{50}^2)$  are typically more than one order of magnitude larger, and comparable to those found for low-redshift LyC leakers and SFGs at high redshifts (Curtis-Lake et al. 2016; Paulino-Afonso et al. 2018; Bouwens et al. 2017).

#### 6 LY $\alpha$ EMISSION

The rest-frame Ly $\alpha$  profiles in the medium-resolution spectra of the 9 xLAEs are shown in Fig. 4. A double-peaked Ly $\alpha$  emission line is detected in the spectra of all galaxies. In two galaxies, J0122+0048 and J1206+5007, the line is weak and in J0122+0048, it is superposed on a broad absorption line. In the remaining seven xLAEs, a strong Ly $\alpha$   $\lambda$ 1216 Å emission-line is seen, with the most intense one in J2229+2725. The two-peak shape is similar to that observed in known LyC leakers (Izotov et al. 2016a,b, 2018a,b; Verhamme et al. 2017) and in GP galaxies (Jaskot & Oey 2014; Henry et al. 2015; Yang et al. 2017; McKinney et al. 2019). Some parameters of the Ly $\alpha$  emission line such as flux, luminosity, equivalent width and separation between the peaks are presented in Table 6.

One of the goals of this paper is to derive for each galaxy the escape fraction of the Ly $\alpha$  emission, and indirectly the absolute escape fraction of the Lyman continuum. To achieve such a goal, some characteristics derived from the optical spectra should be used, e.g. the fluxes of the H $\beta$  emission line. However, observations in the UV and optical ranges were obtained with different telescopes and somewhat different spectroscopic apertures. Therefore, for the determination of the Ly $\alpha$  and LyC escape fractions, the consistency of the fluxes in the UV and optical ranges should be checked. One approach would be to see how well the extrapolation toward UV wavelengths of the optical spectral energy distribution from the SDSS spectrum would fit the UV COS spectrum. Such a method has been adopted e.g. by Izotov et al. (2018a,b, 2020, 2021a, 2022) and we will use it here.

In Fig. 5, we show the observed COS and SDSS spectra of our sample galaxies (grey lines), together with the

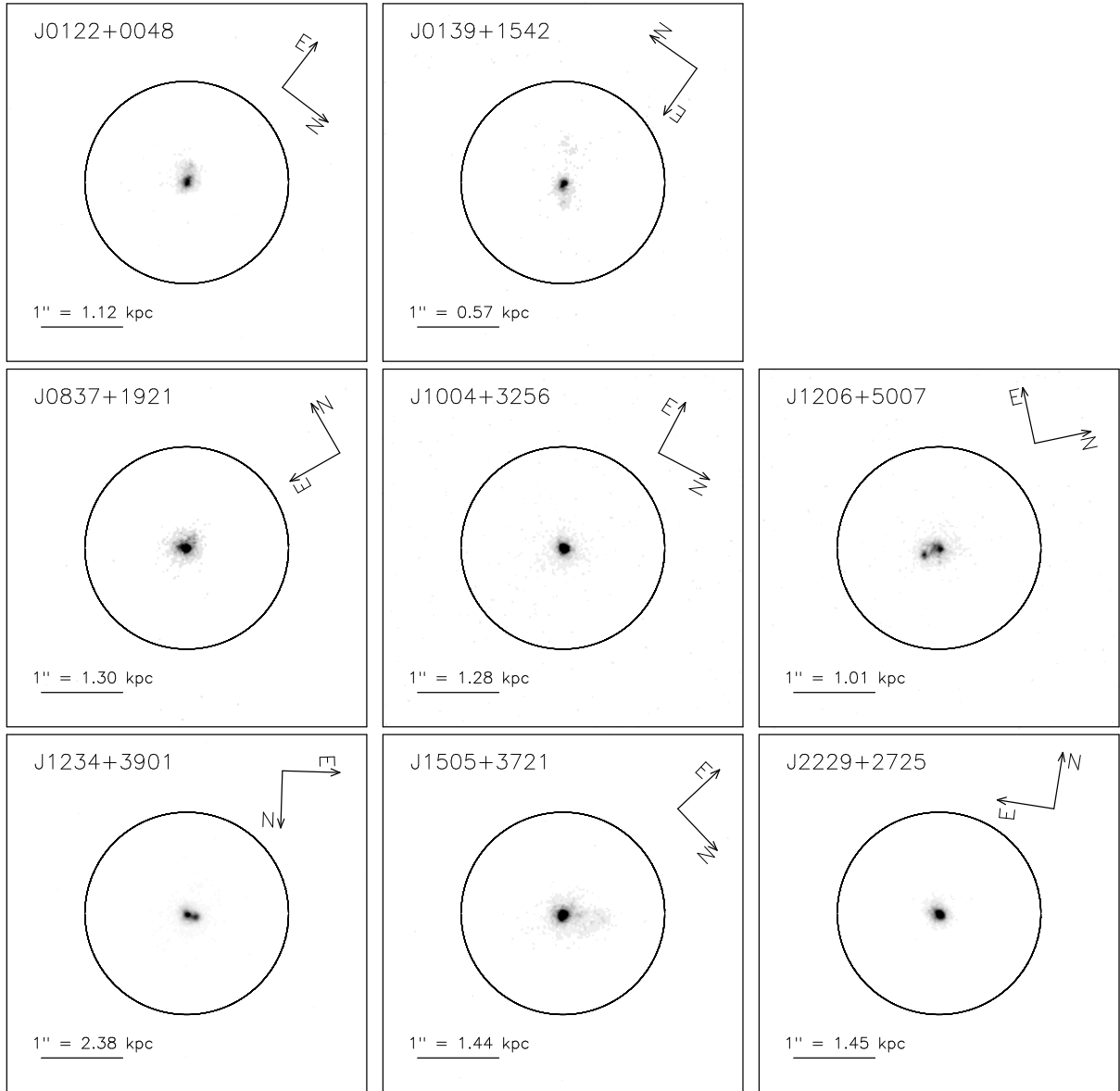


**Figure 2.** The *HST*/COS NUV acquisition images of the most metal-deficient galaxies in log surface brightness scale. The image for J0811+4730 is not shown (see text). A circle in all panels is the COS spectroscopic aperture with a diameter of 2.5 arcsec. The linear scale in each panel is derived adopting the angular size distance (Table 1).

*GALEX* FUV and NUV (magenta filled circles with  $1\sigma$  errors) and SDSS  $u, g, r, i, z$  apparent magnitudes (blue filled circles). These photometric measurements are superposed on the reddened modelled SEDs of the optical spectra and the SED extrapolations to the UV range. For the reddened SEDs we adopt the extinction coefficients derived from the observed hydrogen Balmer decrements and the reddening laws by Cardelli et al. (1989) with  $R(V) = 2.7$  and 3.1 (red and black lines, respectively, in Fig. 5).

Several remarks can be made. First, we note that the SDSS spectra are consistent with the total SDSS magnitudes, indicating that our galaxies are very compact and that all the galaxy light falls into the spectroscopic SDSS aperture. Therefore, aperture corrections are not needed. Second, the red and black lines are nearly coincident because of the small extinction. Third, the reddened SEDs satisfac-

torily reproduce both the observed UV and optical spectra. Therefore, we can directly use extinction-corrected Ly $\alpha$  and H $\beta$  fluxes to derive the Ly $\alpha$  escape fraction, without any additional correction to adjust the UV COS spectrum to the extrapolation of the optical SED. On the other hand, we note that the flux densities derived from the *GALEX* FUV and NUV magnitudes (magenta symbols in Fig. 5) are poorly consistent with the flux densities of the COS spectra. Similar discrepancies were noted earlier by Izotov et al. (2016b, 2018a,b, 2021a, 2022) in low- $z$  LyC galaxies. This indicates that *GALEX* FUV and NUV magnitudes should not be used in general for accurate SED fitting, at least for faint galaxies with COS observations.



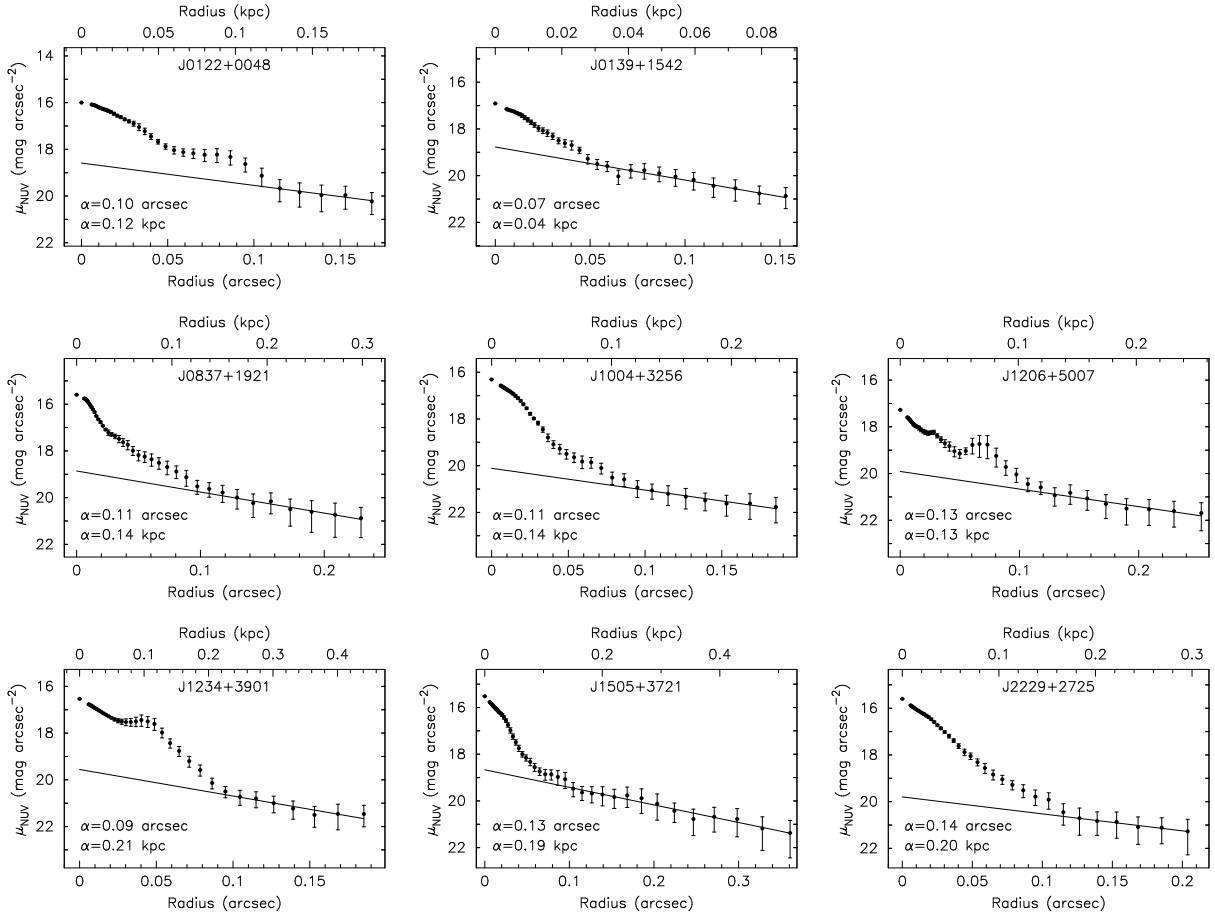


**Figure 3.** NUV surface brightness profiles of the most metal-deficient galaxies. The profile for J0811+4730 is not shown. Solid lines represent the linear fits to the surface brightness profiles of the outer galaxy parts.

**Table 6.** Parameters for the Ly $\alpha$  and H $\beta$  emission lines

Name	$A(\text{Ly}\alpha)_{\text{MW}}^{\text{a}}$	$I(\text{Ly}\alpha)^{\text{b}}$	$\log L(\text{Ly}\alpha)^{\text{c}}$	$\text{EW}(\text{Ly}\alpha)^{\text{d}}$	$V_{\text{sep}}^{\text{e}}$	$I(\text{H}\beta)^{\text{f}}$	$f_{\text{esc}}(\text{Ly}\alpha)^{\text{g}}$	$f_{\text{esc}}(\text{LyC})^{\text{h}}$
J0122+0048	0.291	10.6 $\pm$ 4.9	39.93 $\pm$ 0.17	14.1 $\pm$ 5.5	671.2 $\pm$ 51.3	8.7 $\pm$ 0.5	5.2 $\pm$ 2.4	1.0 $\pm$ 0.5
J0139+1542	0.500	121.4 $\pm$ 5.3	40.35 $\pm$ 0.02	171.2 $\pm$ 7.5	252.0 $\pm$ 26.1	7.8 $\pm$ 0.5	66.8 $\pm$ 5.2	18.7 $\pm$ 1.5
J0811+4730	0.595	272.4 $\pm$ 7.7	41.11 $\pm$ 0.01	187.7 $\pm$ 5.3	365.5 $\pm$ 22.6	13.4 $\pm$ 1.8	87.2 $\pm$ 12.0	5.0 $\pm$ 0.7
J0837+1921	0.220	151.8 $\pm$ 5.8	41.23 $\pm$ 0.02	131.6 $\pm$ 5.0	260.6 $\pm$ 43.5	7.9 $\pm$ 0.6	82.5 $\pm$ 7.0	16.8 $\pm$ 1.4
J1004+3256	0.138	310.4 $\pm$ 6.3	41.53 $\pm$ 0.01	239.9 $\pm$ 4.9	350.7 $\pm$ 47.1	25.3 $\pm$ 1.1	52.7 $\pm$ 2.5	5.8 $\pm$ 0.3
J1206+5007	0.164	17.1 $\pm$ 5.9	40.03 $\pm$ 0.13	15.2 $\pm$ 5.2	548.3 $\pm$ 59.0	9.9 $\pm$ 0.7	7.4 $\pm$ 2.6	1.0 $\pm$ 0.4
J1234+3901	0.123	233.8 $\pm$ 8.0	42.05 $\pm$ 0.01	174.8 $\pm$ 6.0	292.9 $\pm$ 11.2	17.3 $\pm$ 1.0	58.0 $\pm$ 3.9	11.3 $\pm$ 0.8
J1505+3721	0.145	53.4 $\pm$ 9.9	40.88 $\pm$ 0.07	57.4 $\pm$ 9.9	369.9 $\pm$ 17.8	30.6 $\pm$ 1.1	7.5 $\pm$ 1.4	4.7 $\pm$ 0.9
J2229+2725	0.419	301.8 $\pm$ 7.8	41.64 $\pm$ 0.01	178.2 $\pm$ 4.6	207.0 $\pm$ 16.2	20.4 $\pm$ 0.8	63.5 $\pm$ 3.0	34.2 $\pm$ 1.6

<sup>a</sup> $A(\text{Ly}\alpha)_{\text{MW}}$  is the Milky Way extinction at the observed wavelength of the Ly $\alpha$  emission line in mags, adopting [Cardelli et al. \(1989\)](#) reddening law with  $R(V)=3.1$ .

<sup>b</sup> $I(\text{Ly}\alpha)$  is the Ly $\alpha$  flux density in  $10^{-16}$  erg s $^{-1}$  cm $^{-2}$  measured in the COS spectrum and corrected for the Milky Way extinction.

<sup>c</sup> $L(\text{Ly}\alpha)$  is the Ly $\alpha$  luminosity in erg s $^{-1}$  corrected for the Milky Way extinction.

<sup>d</sup> $\text{EW}(\text{Ly}\alpha)$  is the rest-frame equivalent width in  $\text{\AA}$  of the Ly $\alpha$  emission line.

<sup>e</sup> $V_{\text{sep}}$  is the Ly $\alpha$  velocity peak separation in km s $^{-1}$ .

<sup>f</sup> $I(\text{H}\beta)$  is the extinction-corrected H $\beta$  flux density in  $10^{-16}$  erg s $^{-1}$  cm $^{-2}$  measured in the SDSS spectrum.

<sup>g</sup> $f_{\text{esc}}(\text{Ly}\alpha)$  is the ratio in percentage of  $I(\text{Ly}\alpha)/I(\text{H}\beta)$  to its case B value of 23.3.

<sup>h</sup> $f_{\text{esc}}(\text{LyC})$  is the indirectly derived LyC escape fraction in percentage, using the value of  $V_{\text{sep}}$  and equation 2 in [Izotov et al. \(2018b\)](#).

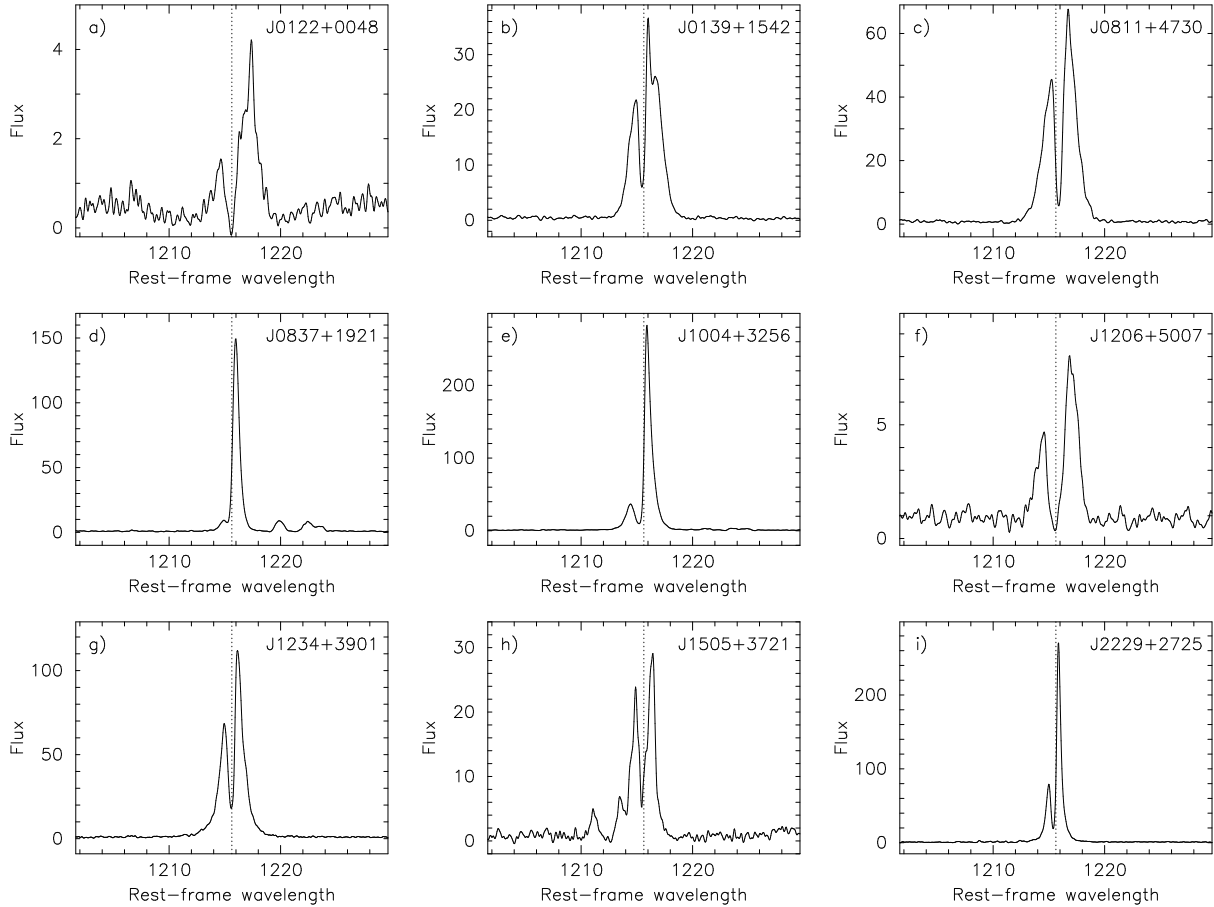


**Figure 4.** Ly $\alpha$  profiles. Vertical dotted lines indicate the centres of profiles. The geocoronal O I  $\lambda$ 1301,1304Å emission in spectra was removed by considering only orbital night data in the affected wavelength range. The removal of these lines is most important for J1505+3721 and J2229+2725 as they are very close to or overlapping with the Ly $\alpha$  emission line. Flux densities are in  $10^{-16}$  erg s $^{-1}$  cm $^{-2}$ Å $^{-1}$  and wavelengths are in Å.

## 7 DISCUSSION

### 7.1 Dependencies of the Ly $\alpha$ escape fractions on Ly $\alpha$ equivalent widths and peak separations

In this section we consider the properties derived from the Ly $\alpha$  emission of our xLAEs and compare them with the respective properties of the low- $z$  and high- $z$  galaxies from the comparison sample. This sample includes the low- $z$  LyC leaking galaxies from Izotov et al. (2016a,b, 2018a,b, 2021a, 2022), Flury et al. (2022), the low- $z$  LAEs from Izotov et al. (2020), Henry et al. (2015), Jaskot & Oey (2014), Jaskot et al. (2017), Yang et al. (2016, 2017), Xu et al. (2022), Hu et al. (2023), and the high- $z$  LAEs from the papers with references given in Table 4. For all low- $z$  LyC galaxies and LAEs from the comparison sample, we collected and/or derived the same set of characteristics as for xLAEs. All these galaxies have SDSS spectra, allowing to derive some optical characteristics. The data for high- $z$  LAEs are scarcer, with the richest data for the Ly $\alpha$  luminosities and equivalent widths.

In Fig. 6a we display the  $L(\text{Ly}\alpha) - M_{\text{FUV}}$  relation, which shows a decline of the Ly $\alpha$  luminosity toward the fainter galaxies, in line with the similar trend found by Hashimoto et al. (2017). The maximum likelihood fit to all data in the Figure, excluding high- $z$  LAEs (purple stars),

can be expressed as

$$\log L(\text{Ly}\alpha) = -0.34453 \times M_{\text{FUV}} + 35.59659. \quad (1)$$

The xLAEs (black symbols) extend the relation to fainter magnitudes. We also note that faint  $z \gtrsim 6$  LAEs, with  $M_{\text{FUV}} \geq -18$  mag (purple stars), are systematically brighter compared to low- $z$  LAEs. The decline of Ly $\alpha$  luminosity is expected toward fainter small objects. However, it is not as steep as the expected relation with a slope of  $-0.4$  if  $L(\text{Ly}\alpha)$  is just proportional to the UV luminosity. This is because the equivalent widths  $\text{EW}(\text{Ly}\alpha)$  are higher for faint low-mass galaxies (Fig. 6b). The trend of increasing  $\text{EW}(\text{Ly}\alpha)$  with decreasing  $M_{\text{FUV}}$  is also found for bright  $z \gtrsim 6$  galaxies with  $M_{\text{FUV}} < -19$  mag (Jones et al. 2023; Saxena et al. 2023). An extension of the relation in Fig. 6b to fainter magnitudes, including xLAEs, reveals that the Ly $\alpha$  equivalent widths at faint magnitudes  $M_{\text{FUV}} \geq -18$  mag become constant, with the highest values not exceeding  $\sim 250\text{\AA}$ . This is consistent with the maximum Ly $\alpha$  equivalent widths of  $\sim 240 - 350\text{\AA}$  predicted by standard synthesis models for metallicities between solar ( $Z = 0.02$ ) and  $Z = 0.0004$  (Schaerer 2003).

The main goal of this study is to derive the properties of the Ly $\alpha$  emission in galaxies with the lowest known metallicities, and to search for possible dependencies of the derived galaxy characteristics on metallicity. Such charac-

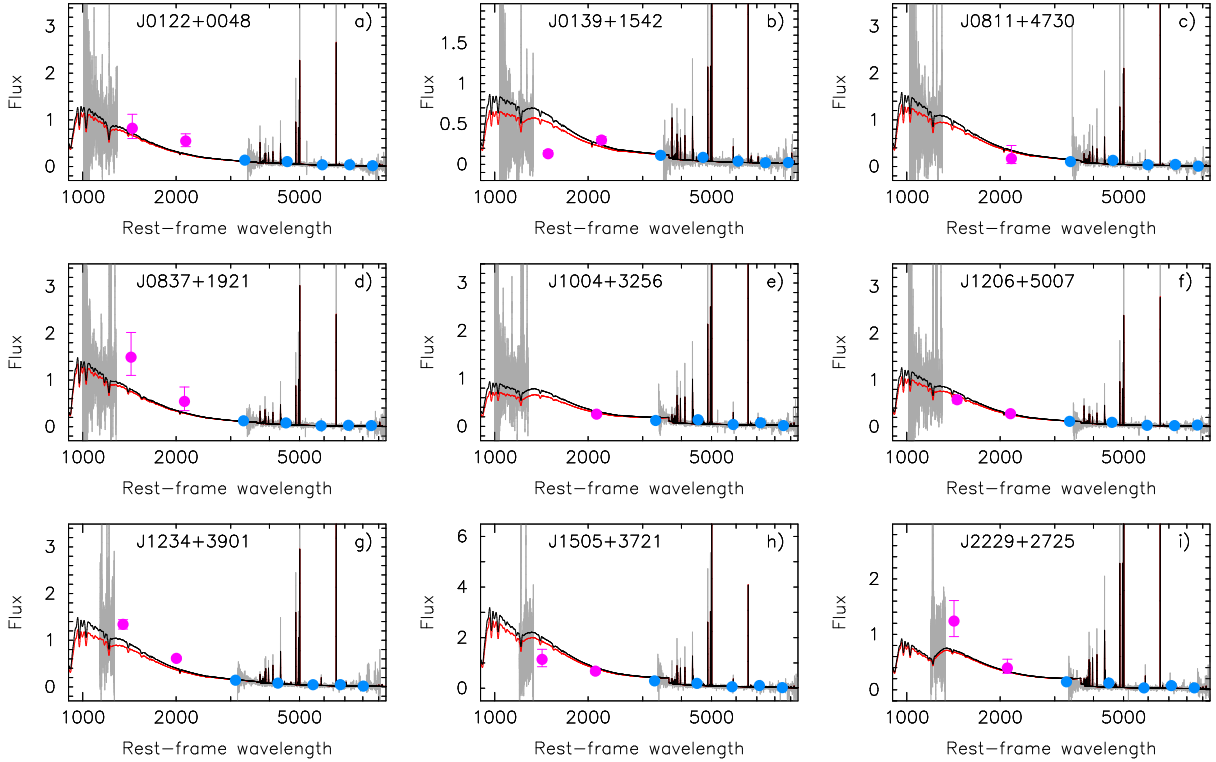


**Figure 5.** A comparison of the COS G130M and SDSS spectra (grey lines), and photometric data with the modelled SEDs. Photometric data for GALEX FUV and NUV fluxes with  $1\sigma$  error bars (magenta symbols) and SDSS fluxes in  $u, g, r, i, z$  bands (blue symbols) are shown. Modelled intrinsic SEDs, which are reddened by the Milky Way extinction using Cardelli et al. (1989) reddening law with  $R(V)_{\text{MW}} = 3.1$  and internal extinction with  $R(V)_{\text{int}} = 3.1$  and  $2.7$ , are shown by black and red solid lines, respectively. Flux densities are in  $10^{-16} \text{ erg s}^{-1} \text{ cm}^{-2} \text{ \AA}^{-1}$ , wavelengths are in  $\text{\AA}$ .

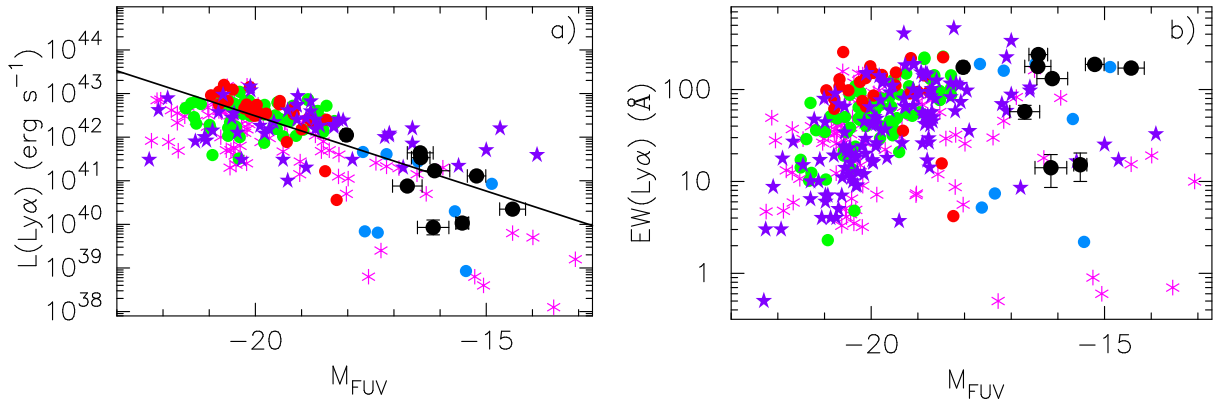


**Figure 6.** Relations between the a) Ly $\alpha$  luminosities  $L(\text{Ly}\alpha)$  and the absolute FUV magnitudes  $M_{\text{FUV}}$  derived from the rest-frame SEDs, b) equivalent widths  $\text{EW}(\text{Ly}\alpha)$  and the absolute FUV magnitudes  $M_{\text{FUV}}$ . The relation in a) is defined by Eq. 1. Meaning of symbols is the same as in Fig. 1.

teristics can be the Ly $\alpha$  luminosity, the equivalent width  $\text{EW}(\text{Ly}\alpha)$ , or the separation  $V_{\text{sep}}$  between the Ly $\alpha$  peaks. In Fig. 7a, we show the relation between oxygen abundance  $12+\log(\text{O}/\text{H})$  and Ly $\alpha$  luminosity  $L(\text{Ly}\alpha)$ . A clear trend of increasing  $L(\text{Ly}\alpha)$  with increasing  $12+\log(\text{O}/\text{H})$  is seen. This trend is somewhat expected because xLAEs being the lowest-mass (Fig. 1c) and faintest galaxies have also the lowest Ly $\alpha$  luminosities (Fig. 6a). On the other hand, there are no evident correlations of  $\text{EW}(\text{Ly}\alpha)$  and  $V_{\text{sep}}$  with  $12+\log(\text{O}/\text{H})$  (Fig. 7b – 7c). Thus, low metallicity

is likely not a good indicator for the selection of galaxies with high LyC leakage. Seven xLAEs are characterised by high  $\text{EW}(\text{Ly}\alpha)$  (Fig. 7b) and small  $V_{\text{sep}}$  (Fig. 7c), classifying them as possible LyC leakers. On the other hand, two xLAEs have low  $\text{EW}(\text{Ly}\alpha)$  and high  $V_{\text{sep}}$ , indicating the presence of optically thick neutral gas in the line of sight between the source of ionizing radiation and the observer.

In Fig. 8 are shown various dependencies of the Ly $\alpha$  escape fraction on diverse characteristics of xLAEs and galaxies from the comparison sample. The escape fraction

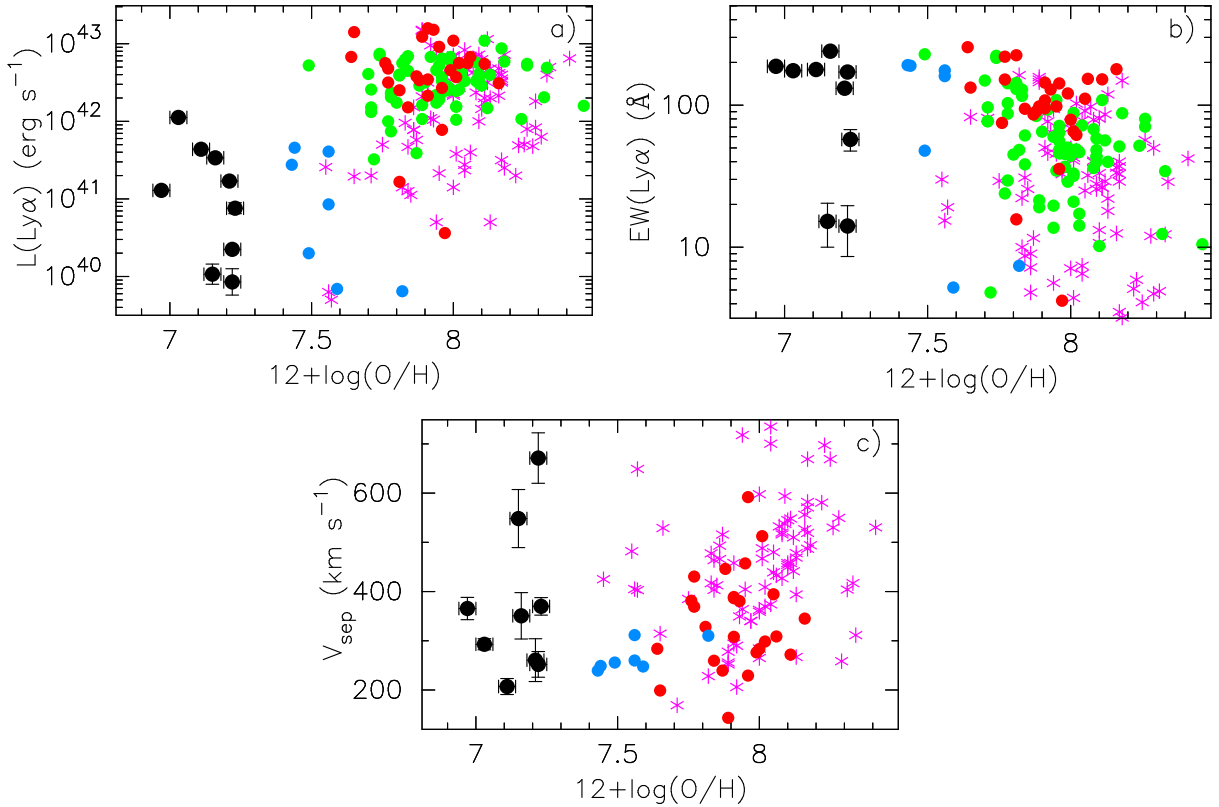


**Figure 7.** Relations between the oxygen abundances and **a)** Ly $\alpha$  luminosities  $L(\text{Ly}\alpha)$ , **b)** Ly $\alpha$  rest-frame equivalent widths  $\text{EW}(\text{Ly}\alpha)$  and **c)** Ly $\alpha$  peak separations  $V_{\text{sep}}$ . Meaning of symbols is the same as in Fig. 1.

$f_{\text{esc}}(\text{Ly}\alpha)$  is defined as the ratio of the extinction-corrected Ly $\alpha$  to H $\beta$  flux ratio to its Case B value of 23.3, corresponding to a low electron number density,  $N_e \sim 10^2 \text{ cm}^{-3}$  (Storey & Hummer 1995):

$$f_{\text{esc}}(\text{Ly}\alpha) = \frac{1}{23.3} \frac{I(\text{Ly}\alpha)}{I(\text{H}\beta)}, \quad (2)$$

where  $I(\text{Ly}\alpha)$  is the flux corrected for the Milky Way extinction, and  $I(\text{H}\beta)$  is the flux corrected for both the Milky Way and internal galaxy extinction.

Eq. 2 was applied to derive  $f_{\text{esc}}(\text{Ly}\alpha)$  for both the xLAE and comparison galaxies. Using both sets of data, we search for possible correlations of  $f_{\text{esc}}(\text{Ly}\alpha)$  with galaxy integrated characteristics. It is seen in Fig. 8 that low- $z$  and high- $z$  LAEs from the comparison sample overlap well, indicating that LAEs at reionization epoch have properties very similar to those of nearby LAEs. An exception is the xLAE sample. Galaxies from this sample are fainter and less massive, with lower metallicities and Ly $\alpha$  luminosities. Other characteristics, such as O $_{32}$  ratios and ionizing photon production efficiencies  $\xi_{\text{ion}}$ , are similar to those of the galaxies in the comparison sample.

We find no or weak correlation between  $f_{\text{esc}}(\text{Ly}\alpha)$  and absolute FUV magnitude  $M_{\text{FUV}}$ , oxygen abundance  $12 + \log(\text{O}/\text{H})$ , O $_{32}$  ratio, stellar mass  $M_*$ , Ly $\alpha$  luminosity and ionizing photon production efficiency. On the other hand, relatively tight correlations are found between  $f_{\text{esc}}(\text{Ly}\alpha)$  and  $\text{EW}(\text{Ly}\alpha)$  (Fig. 8g), and between  $f_{\text{esc}}(\text{Ly}\alpha)$  and  $V_{\text{sep}}$  (Fig. 8h), in accord with the study by Yang et al. (2017). The maximum likelihood relation shown in Fig. 8g by the

dotted line is obtained by including all galaxies. However, the errors of  $\text{EW}(\text{Ly}\alpha)$  and  $f_{\text{esc}}(\text{Ly}\alpha)$  might be very large for galaxies with weak Ly $\alpha$  emission, due to their higher flux uncertainties, as indicated by the larger errors of our xLAEs (black symbols) at low  $\text{EW}(\text{Ly}\alpha)$ . To study the role of these uncertainties on the determination of the maximum likelihood relation, we show in Fig. 8g by a solid line the relation for galaxies with  $\text{EW}(\text{Ly}\alpha) > 10 \text{ \AA}$  and  $f_{\text{esc}}(\text{Ly}\alpha) > 5$  per cent. This relation expressed as

$$\log f_{\text{esc}}(\text{Ly}\alpha) = 0.74851 \times \log \text{EW}(\text{Ly}\alpha) - 1.98411 \quad (3)$$

is nearly coincident with the one for the entire sample. According to Eq. 3, the “intrinsic” Ly $\alpha$  equivalent width defined as  $\text{EW}(\text{Ly}\alpha)/f_{\text{esc}}(\text{Ly}\alpha)$ , i.e. the value of  $\text{EW}(\text{Ly}\alpha)$  corresponding to the Ly $\alpha$  escape fraction of 1, is equal to  $\sim 380 \text{ \AA}$  in galaxies with the high observed  $\text{EW}(\text{Ly}\alpha) = 250 \text{ \AA}$ . This “intrinsic” value is consistent with the values predicted by the population synthesis models (e.g. Schaerer 2003).

The respective correlation between the Ly $\alpha$  peak separations and Ly $\alpha$  escape fractions in Fig. 8h for the restricted sample with  $\text{EW}(\text{Ly}\alpha) > 10 \text{ \AA}$  and  $f_{\text{esc}}(\text{Ly}\alpha) > 5$  per cent can be fit by the maximum likelihood equation in the form:

$$\log f_{\text{esc}}(\text{Ly}\alpha) = -0.00125 \times V_{\text{sep}} - 0.15279. \quad (4)$$

## 7.2 Correlation between the escape fractions of LyC and Ly $\alpha$ emission

It is important for studies of the reionization of the Universe to find correlations between the escape fraction of the

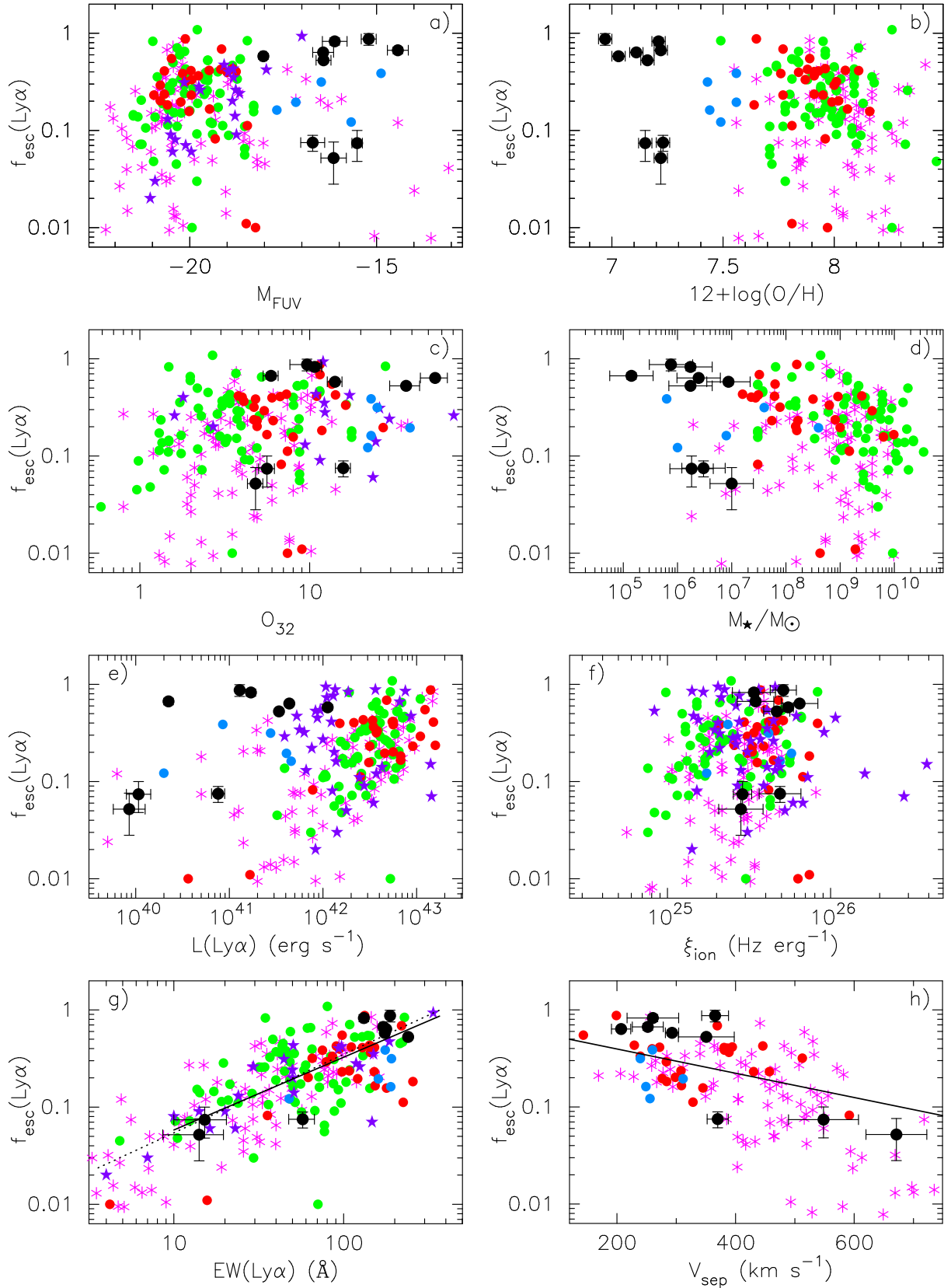


**Figure 8.** Relations between the Ly $\alpha$  escape fractions  $f_{\text{esc}}(\text{Ly}\alpha)$  and various integrated characteristics of the low- and high- $z$  LAEs. Maximum likelihood relations in **g**) and **h**) shown by solid lines are derived for the galaxies with  $\text{EW}(\text{Ly}\alpha) > 10\text{\AA}$  and  $f_{\text{esc}}(\text{Ly}\alpha) > 5$  per cent and are defined by Eqs. 3 and 4, respectively. On the other hand, the relation obtained for all galaxies is shown in **g**) with dotted line. Meaning of symbols is the same as in Fig. 1.

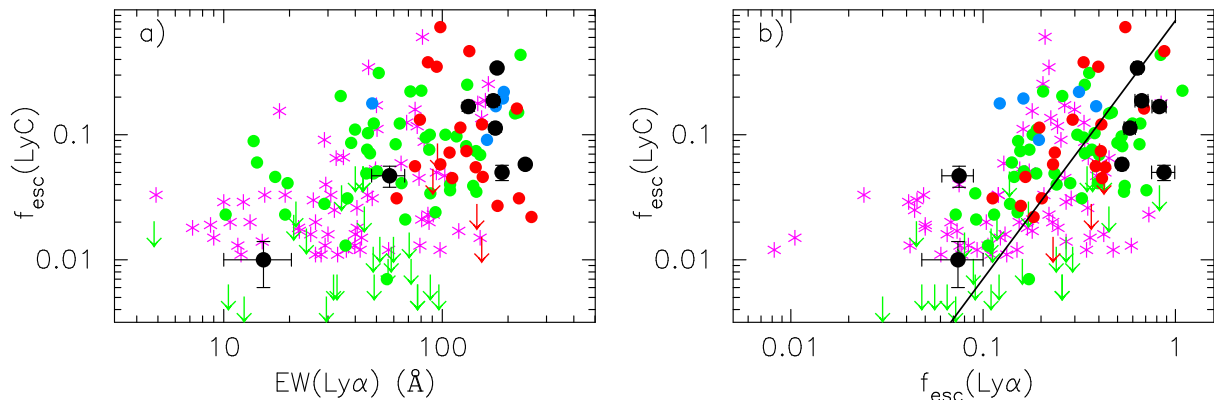


**Figure 9.** Dependencies of the LyC escape fractions  $f_{\text{esc}}(\text{LyC})$  on **a)** equivalent widths of the Ly $\alpha$  emission line and **b)** escape fractions  $f_{\text{esc}}(\text{Ly}\alpha)$  of the Ly $\alpha$  emission line. The maximum likelihood relation in **b)** is derived using only galaxies with direct measurements of the Lyman continuum (red and green circles) and is defined by Eq. 5. Filled red and green circles represent galaxies with detected Lyman continuum and arrows are for the galaxies with upper limits, respectively. The escape fractions of the Lyman continuum shown by blue, magenta and black symbols are derived using equation 2 by Izotov et al. (2018b) and excluding galaxies with  $V_{\text{sep}} > 500 \text{ km s}^{-1}$ .

LyC emission  $f_{\text{esc}}(\text{LyC})$  and some characteristics of the Ly $\alpha$  emission line. One of the most commonly measured characteristics is the equivalent width  $\text{EW}(\text{Ly}\alpha)$  of the Ly $\alpha$  emission line. As for  $f_{\text{esc}}(\text{LyC})$ , it can be obtained from the observed flux of the LyC emission in the COS spectra of the galaxies with  $z \sim 0.3 - 0.4$ . Concerning galaxies with  $z < 0.3$ , for which direct measurements of the LyC fluxes in the *HST*/COS spectra are not possible, the relation between the  $f_{\text{esc}}(\text{LyC})$  and the Ly $\alpha$  peak separation can be used (e.g. Izotov et al. 2018b).

In Fig. 9a, we show the relation between  $f_{\text{esc}}(\text{LyC})$  and  $\text{EW}(\text{Ly}\alpha)$  for the low- $z$  LyC leakers at  $z \sim 0.3 - 0.4$  and LAEs at  $z \lesssim 0.3$ , including our xLAEs. It is seen that the correlation between  $f_{\text{esc}}(\text{LyC})$  and  $\text{EW}(\text{Ly}\alpha)$  is weak. We conclude that  $\text{EW}(\text{Ly}\alpha)$  is a poor indicator of LyC escaping emission. The Figure allows also to conclude that LAEs with  $\text{EW}(\text{Ly}\alpha) \lesssim 20 \text{ \AA}$  are mainly non-leakers.

A tighter correlation is found between  $f_{\text{esc}}(\text{LyC})$  and  $f_{\text{esc}}(\text{Ly}\alpha)$  (Fig. 9b), where  $f_{\text{esc}}(\text{Ly}\alpha)$  is derived from the extinction-corrected flux ratios of the Ly $\alpha$  and H $\beta$  emission lines (Eq. 2). In this Figure, direct observations of the Lyman continuum are available for galaxies shown by red and green filled circles (LyC is detected) and arrows (upper limits of the LyC fluxes). For the remaining galaxies shown by blue, magenta and black symbols, the LyC escape fraction is derived indirectly with the use of equation 2 by Izotov et al. (2018b). We note however that the peak separations for all galaxies but one, used in the determination of this relation, are less than  $500 \text{ km s}^{-1}$ . Thus, the indirectly derived LyC escape fraction in galaxies with  $V_{\text{sep}} > 500 \text{ km s}^{-1}$  may be badly determined and we excluded these galaxies in Fig. 9b. The maximum likelihood relation in this Figure (solid line) is derived only for galaxies with direct measurements of LyC (red and green filled and open circles). This relation takes the form:

$$\log f_{\text{esc}}(\text{LyC}) = 2.06473 \times \log f_{\text{esc}}(\text{Ly}\alpha) - 0.08773. \quad (5)$$

The distribution of galaxies with indirect determinations of  $f_{\text{esc}}(\text{LyC})$  is similar to the distribution of galaxies with direct measurements of the Lyman continuum fluxes. It follows from Eq. 5 that  $f_{\text{esc}}(\text{LyC})$  is always lower than  $f_{\text{esc}}(\text{Ly}\alpha)$ ,

in agreement with conclusions by Verhamme et al. (2017) and Izotov et al. (2021a), theoretical predictions by Dijkstra, Gronke & Venkatesan (2016) and numerical simulations by Maji et al. (2022). The relation Eq. 5 can be used to determine  $f_{\text{esc}}(\text{LyC})$  in the cases when direct measurements of the LyC fluxes are not possible and resolved Ly $\alpha$  profiles, needed for the determination of  $V_{\text{sep}}$ , are not available. We note, however, that this relation may not be valid if the opacity of the intergalactic medium in the direction of the galaxy is high.

## 8 CONCLUSIONS

We present here *HST*/COS observations of nine low-redshift ( $z \lesssim 0.13$ ) most metal-deficient compact star-forming galaxies (SFG), with oxygen abundances  $12+\log(\text{O}/\text{H})$  in the range  $6.97 - .23$ . All studied objects are compact and low-mass ( $\log(M_*/M_\odot) = 5.2 - 7.0$ ). They show strong nebular emission lines in their optical spectra ( $\text{EW}(\text{H}\beta) = 134 - 580 \text{ \AA}$ ), indicating very young starburst ages of  $< 4 \text{ Myr}$ . We use these data to study the Ly $\alpha$  emission and indirect indicators of the escaping Lyman continuum (LyC) radiation of these SFGs. We compare their properties with those of the low- $z$  LyC galaxies and LAEs and high- $z$  ( $z > 6$ ) LAEs, gathered from the literature. Our main results are summarized as follows:

1. A Ly $\alpha$  emission line with two peaks was observed in the spectra of all galaxies, classifying them as LAEs. This line is strong in seven galaxies, with high equivalent widths  $\text{EW}(\text{Ly}\alpha) \gtrsim 60 \text{ \AA}$ . Our extremely low-metallicity LAEs (xLAEs) considerably extend the range of physical properties of LAEs to a faint UV magnitude of  $-14 \text{ mag}$ , a low stellar mass of  $10^5 M_\odot$  and a low metallicity  $12+\log(\text{O}/\text{H}) \sim 7.0$ , the lowest known so far.

2. We discuss various indirect indicators of escaping Ly $\alpha$  and ionizing radiation. We find correlations between the Ly $\alpha$  escape fractions and the equivalent widths  $\text{EW}(\text{Ly}\alpha)$  and the velocity separations  $V_{\text{sep}}$  between the two peaks of the Ly $\alpha$  profile. We conclude that both  $\text{EW}(\text{Ly}\alpha)$  and  $V_{\text{sep}}$  can be used as secondary indicators to determine  $f_{\text{esc}}(\text{Ly}\alpha)$ . How-

ever, there is no correlation between oxygen abundances and Ly $\alpha$  escape fractions.

3. We also find a correlation between the Ly $\alpha$  and LyC escape fractions, which allows to estimate the LyC escape fractions when direct observations of the Lyman continuum are not possible with the *HST*, e.g. in low- $z$  LAEs with  $z \leq 0.3$ .

4. All our xLAEs are very compact in the COS near ultraviolet (NUV) acquisition images. The surface brightness profiles at the outskirts of these galaxies can be approximated by an exponential disc profile, with a scale length of  $\sim 0.04 - 0.21$  kpc. These scale lengths are several times lower than those of confirmed LyC leakers and are among the lowest ones found for local blue compact dwarf galaxies.

5. We find that the global properties of low- $z$  LAEs are very similar to those of  $z > 6$  galaxies. They are thus ideal nearby laboratories for investigating the mechanisms responsible for the escape of Ly $\alpha$  and ionizing radiation from galaxies during the epoch of the reionization of the Universe.

## ACKNOWLEDGEMENTS

These results are based on observations made with the NASA/ESA *Hubble Space Telescope*, obtained from the data archive at the Space Telescope Science Institute. STScI is operated by the Association of Universities for Research in Astronomy, Inc. under National Aeronautics and Space Administration (NASA) contract NAS 5-26555. Support for T.X.T. was provided by NASA through grant number HST-GO-16672.002-A from the Space Telescope Science Institute. Y.I.I. and N.G.G. acknowledge support from the National Academy of Sciences of Ukraine (Project No. 0123U102248) and from the Simons Foundation. IRAF is distributed by the National Optical Astronomy Observatories, which are operated by the Association of Universities for Research in Astronomy, Inc., under cooperative agreement with the National Science Foundation. STSDAS is a product of the Space Telescope Science Institute, which is operated by AURA for NASA. Funding for the Sloan Digital Sky Survey IV has been provided by the Alfred P. Sloan Foundation, the U.S. Department of Energy Office of Science, and the Participating Institutions. SDSS-IV acknowledges support and resources from the Center for High-Performance Computing at the University of Utah. The SDSS web site is [www.sdss.org](http://www.sdss.org). SDSS-IV is managed by the Astrophysical Research Consortium for the Participating Institutions of the SDSS Collaboration. *Galaxy Evolution Explorer (GALEX)* is a NASA mission managed by the Jet Propulsion Laboratory. This research has made use of the NASA/Infrared Processing and Analysis Center (IPAC) Extragalactic Database (NED) which is operated by the Jet Propulsion Laboratory, California Institute of Technology, under contract with the National Aeronautics and Space Administration. This publication makes use of data products from the *Wide-field Infrared Survey Explorer (WISE)*, which is a joint project of the University of California, Los Angeles, and the Jet Propulsion Laboratory, California Institute of Technology, funded by the National Aeronautics and Space Administration.

## DATA AVAILABILITY

The data underlying this article will be shared on reasonable request to the corresponding author.

## REFERENCES

- Ade P. A. R. et al., 2014, *A&A*, 571, 16  
 Ahumada R. et al. 2020, *ApJS*, 249, 1  
 Asplund M., Grevesse N., Sauval A. J., Scott P., 2009, *ARA&A*, 47, 481  
 Atek H. et al., 2023, preprint arXiv:2308.08540  
 Baldwin J. A., Phillips M. M., Terlevich R., 1981, *PASP*, 93, 5  
 Blaizot J. et al., 2023, *MNRAS*, 523, 3749  
 Borthakur S., Heckman T. M., Leitherer C., Overzier R. A., 2014, *Science*, 346, 216  
 Bouwens R. J., Illingworth G. D., Oesch P. A., Caruana J., Holwerda B., Smit R., Wilkins S., 2015, *ApJ*, 811, 140  
 Bouwens R. J., Smit R., Labbé I., Franx M., Caruana J., Oesch P., Stefanon M., Rasappu N. 2016, *ApJ*, 831, 176  
 Bouwens R. J., Illingworth G. D., Oesch P. A., Atek H, Lam D, Stefanon M., 2017, *ApJ*, 843, 41  
 Cardelli J. A., Clayton G. C., Mathis J. S., 1989, *ApJ*, 345, 245  
 Chen Z., Stark D. P., Endsley R., Topping M., Whitler L., Charlot S., 2023, *MNRAS*, 518, 5607  
 Curti M. et al., 2023, *MNRAS*, 518, 425  
 Curtis-Lake E. et al., 2016, *MNRAS*, 457, 440  
 Dijkstra M., Gronke M., Venkatesan A., 2016, *ApJ*, 828, 71  
 Endsley R., Stark D. P., Whitler L., Topping M. W., Chen Z., Plat A., Chisholm J., Charlot S., 2023a, *MNRAS*, 524, 2312  
 Endsley R. et al., 2023b, preprint arXiv:2306.05295  
 Erb D. K., Steidel C. C., Chen Y., 2018, *ApJ*, 862, 10  
 Flury S. R. et al. 2022, *ApJ*, 930, 126  
 Fujimoto S. et al., 2023, *ApJ*, 949, L25  
 Fuller S. et al., 2020, *ApJ*, 896, 156  
 Hashimoto T. et al., 2017, *A&A*, 608, 10  
 Heintz K. E. et al., 2022, preprint arXiv:2212.02890  
 Henry A., Scarlata C., Martin C. S., Erb D., 2015, *ApJ*, 809, 19  
 Hu W. et al., 2023, preprint arXiv:2307.04911  
 Izotov Y. I., Thuan T. X., Lipovetsky V. A., 1994, *ApJ*, 435, 647  
 Izotov Y. I., Stasińska G., Meynet G., Guseva N. G., Thuan T. X., 2006, *A&A*, 448, 955  
 Izotov Y. I., Orlitová I., Schaerer D., Thuan T. X., Verhamme A., Guseva N. G., Worseck G., 2016a, *Nature*, 529, 178  
 Izotov Y. I., Schaerer D., Thuan, T. X., Worseck G., Guseva N. G., Orlitová I., Verhamme A., 2016b, *MNRAS*, 461, 3683  
 Izotov Y. I., Schaerer D., Worseck G., Guseva N. G., Thuan, T. X., Verhamme A., Orlitová I., Fricke K. J., 2018a, *MNRAS*, 474, 4514  
 Izotov Y. I., Worseck G., Schaerer D., Guseva N. G., Thuan, T. X., Fricke K. J., Verhamme A., Orlitová I., 2018b, *MNRAS*, 478, 4851  
 Izotov Y. I., Thuan T. X., Guseva N. G., Liss S. E., 2018c, *MNRAS*, 473, 1956  
 Izotov Y. I., Thuan T. X., Guseva N. G., 2019, *MNRAS*, 483, 5491  
 Izotov Y. I., Schaerer D., Worseck G., Verhamme A., Guseva N. G., Thuan T. X., Orlitova I., Fricke, K. J. 2020, *MNRAS*, 491, 468  
 Izotov Y. I., Worseck G., Schaerer D., Guseva N. G., Chisholm J., Thuan T. X., Fricke K. J., Verhamme A. 2021a, *MNRAS*, 503, 1734  
 Izotov Y. I., Guseva N. G., Fricke K. J., Henkel C., Schaerer D., Thuan T. X. 2021b, *A&A*, 646, 138  
 Izotov Y. I., Thuan T. X., Guseva N. G., 2021c, *MNRAS*, 504, 3996

- Izotov Y. I., Chisholm J., Worseck G., Guseva N. G., Schaerer D., Prochaska J. X. 2022, MNRAS, 515, 2864
- James B. L., Aloisi A., Heckman T., Sohn S. T., Wolfe M. A., 2014, ApJ, 795, 109
- Jaskot A. E., Oey M. S., 2014, ApJ, 791, L19
- Jaskot A. E., Oey M. S., Scarlata C., Dowd T., 2017, ApJ, 851, L9
- Jiang L. et al., 2018, ApJ, 772, 99
- Jones T. et al., ApJ, 903,150
- Jones G. C. et al., 2023, preprint arXiv:2306.02471
- Jung I. et al., 2022, preprint arXiv:2212.09850
- Jung I. et al., 2023, preprint arXiv:2304.05385
- Kashikawa N. et al., 2011, ApJ, 734, 119
- Kauffmann G. et al., 2003, MNRAS, 341, 33
- Kennicutt R. C., Jr., 1998, ARA&A, 36, 189
- Kikuchihara S. et al., 2020, ApJ, 893, 60
- Kimm T., Blaizot J., Carel T., Michel-Danzac L., Katz H., Rosdahl J., Verhamme A., Haehnelt M., 2019, MNRAS, 486, 2215
- Kulkarni G., Worseck G., Hennawi J. F., 2019, MNRAS, 488, 1035
- Langan I., Severino D., Finlator K., 2020, MNRAS, 494, 1988
- Langeroodi D. et al. 2022, preprint arXiv:2212.02491
- Lin Y.-H. et al., 2023, preprint arXiv:2303.04572
- Macsia S. et al., 2023, A&A, 672, 155
- Madau P., Pozzetti L., Dickinson M., 1998, ApJ, 498, 106
- Maji M. et al., 2022, A&A, 663, 66
- Makan K., Worseck G., Davies F. B., Hennawi J. F., Prochaska J. X., Richter P., 2021, ApJ, 912, 38
- Matthee J., Mackenzie R., Simcoe R. A., Kashino D., Lilly S. J., Bordoloi R., Eilers A.-C. 2023, ApJ, 950, 67
- McKinney J. H., Jaskot A. E., Oey M. S., Yun M. S., Dowd T., Lowenthal J. D., 2019, ApJ, 874, 52
- Mitra S., Ferrara A., Choudhury T. R., 2013, MNRAS, 428, L1
- Naidu R. P., Forrest B., Oesch P. A., Tran K.-V. H., Holden B. P., 2018, MNRAS, 478, 791
- Ning Y., Cai Z., Jiang L., Lin X., Fu S., Spinoso D., 2023, ApJ, 944, 1
- Ouchi M. et al., 2008, ApJS, 176, 301
- Ouchi M. et al., 2009, ApJ, 706, 1136
- Papaderos P., Izotov Y. I., Thuan T. X., Noeske K. G., Fricke K. J., Guseva N. G., Green R. F., 2002, A&A, 393, 461
- Paulino-Afonso A. et al., 2018, MNRAS, 476, 5479
- Pentericci L. et al., 2018, A&A, 619, 147
- Rhoads J. E. et al., 2023, ApJ, 942, L14
- Rivera-Thorsen T. E. et al., 2017, A&A, 608, L4
- Robertson B. E. et al., 2013, ApJ, 768, 71
- Santini P. et al., 2023, ApJ, 942, 27
- Saxena A. et al., 2023, preprint arXiv:2306.04536
- Schaerer D., 2003, A&A, 397, 527
- Schaerer D., Marques-Chaves R., Barrufet L., Oesch P., Izotov Y. I., Naidu R., Guseva N. G., Brammer G., 2022, A&A, 665, L4
- Shapley A. E., Reddy N. A., Ryan L., Sanders R. L., Topping M. W., Brammer G. B. 2023, ApJ, 950, L1
- Simmonds C. et al., 2023, MNRAS, 523, 5468
- Smith B. M. et al., 2018, ApJ, 853, 191
- Steidel C. C., Bogosavljević M., Shapley A.E., Reddy N. A., Rudie G. C., Pettini M., Trainor R. F., Strom A. L., 2018, ApJ, 869, 123
- Storey P. J., Hummer D. G., 1995, MNRAS, 272, 41
- Tang M. et al., 2023, MNRAS, 526, 1657
- Trump J. R. et al., 2023, ApJ, 945, 35
- Vanzella E. et al., 2018, MNRAS, 476, L15
- Verhamme A., Orlitová I., Schaerer D., Hayes M., 2015, A&A, 578, 7
- Verhamme A., Orlitová I., Schaerer D., Izotov Y., Worseck G., Thuan T. X., Guseva N., 2017, A&A, 597, 13
- Wise J. H., Cen R., 2009, ApJ, 693, 984
- Wright E. L., 2006, PASP, 118, 1711
- Xu X. et al., 2022, ApJ, 993, 202
- Yajima H., Choi J.-H., Nagamine K., 2011, MNRAS, 412, 411
- Yang H., Malhotra S., Gronke M., Rhoads J. E., Dijkstra M., Jaskot A., Zheng Z., Wang J., 2016, ApJ, 820, 130
- Yang H. et al., 2017, ApJ, 844, 171

## APPENDIX A: EMISSION-LINE FLUXES IN SDSS SPECTRA AND ELEMENT ABUNDANCES

This paper has been typeset from a  $\text{\TeX}/\text{\LaTeX}$  file prepared by the author.



**Table A1.** Extinction-corrected emission-line fluxes in SDSS spectra

Line	$\lambda$	$100 \times I(\lambda)/I(H\beta)^a$					
		J0122+0048	J0139+1542	J0811+4730	J0837+1921	J1004+3256	
[O II]	3727	51.6 $\pm$ 5.5	50.3 $\pm$ 4.7	17.3 $\pm$ 3.0	33.1 $\pm$ 4.9	9.0 $\pm$ 1.9	
H12	3750	...	...	...	...	...	
H11	3771	...	...	...	...	5.3 $\pm$ 1.4	
H10	3798	...	...	6.9 $\pm$ 2.7	...	8.0 $\pm$ 1.6	
H9	3836	...	...	8.2 $\pm$ 2.6	...	8.2 $\pm$ 1.6	
[Ne III]	3869	22.6 $\pm$ 4.0	30.6 $\pm$ 3.9	14.7 $\pm$ 2.9	36.9 $\pm$ 4.8	31.2 $\pm$ 2.7	
H8+He I	3889	25.3 $\pm$ 4.1	21.9 $\pm$ 3.3	22.0 $\pm$ 3.1	20.6 $\pm$ 3.9	20.5 $\pm$ 2.2	
H7+[Ne III]	3969	26.9 $\pm$ 4.1	26.3 $\pm$ 3.6	32.4 $\pm$ 3.7	20.0 $\pm$ 3.8	28.0 $\pm$ 2.5	
H $\delta$	4101	29.0 $\pm$ 4.1	29.2 $\pm$ 3.4	27.5 $\pm$ 3.3	31.5 $\pm$ 4.4	29.2 $\pm$ 2.5	
H $\gamma$	4340	49.2 $\pm$ 4.9	50.4 $\pm$ 4.4	49.3 $\pm$ 4.1	51.9 $\pm$ 5.2	47.5 $\pm$ 3.1	
[O III]	4363	9.4 $\pm$ 3.0	12.9 $\pm$ 2.6	6.5 $\pm$ 2.0	16.8 $\pm$ 3.4	15.2 $\pm$ 1.8	
He I	4471	...	4.1 $\pm$ 2.2	3.6 $\pm$ 1.6	...	3.7 $\pm$ 1.1	
He II	4686	...	...	2.3 $\pm$ 1.1	7.7 $\pm$ 2.8	1.7 $\pm$ 1.0	
H $\beta$	4861	100.0 $\pm$ 6.6	100.0 $\pm$ 5.8	100.0 $\pm$ 5.6	100.0 $\pm$ 6.9	100.0 $\pm$ 4.4	
[O III]	4959	86.1 $\pm$ 6.1	100.0 $\pm$ 5.8	57.9 $\pm$ 4.2	116.0 $\pm$ 7.3	116.1 $\pm$ 4.8	
[O III]	5007	247.5 $\pm$ 10.8	297.9 $\pm$ 11.0	166.0 $\pm$ 7.4	353.0 $\pm$ 14.1	332.7 $\pm$ 9.2	
He I	5876	10.7 $\pm$ 2.5	15.0 $\pm$ 2.1	8.7 $\pm$ 1.7	9.8 $\pm$ 2.3	11.3 $\pm$ 1.4	
[O I]	6300	1.3 $\pm$ 1.6	...	1.3 $\pm$ 0.7	...	...	
[S III]	6312	0.6 $\pm$ 1.4	...	...	...	...	
H $\alpha$	6563	274.1 $\pm$ 12.1	275.6 $\pm$ 10.7	275.3 $\pm$ 10.6	270.4 $\pm$ 12.4	149.1 $\pm$ 5.8 <sup>b</sup>	
[N II]	6583	2.7 $\pm$ 1.6	3.0 $\pm$ 1.1	0.6 $\pm$ 0.7	1.8 $\pm$ 1.6	0.4 $\pm$ 0.3	
He I	6678	...	3.1 $\pm$ 1.2	2.4 $\pm$ 1.0	...	2.5 $\pm$ 0.7	
[S II]	6717	3.8 $\pm$ 1.7	6.1 $\pm$ 1.5	1.8 $\pm$ 1.0	...	1.2 $\pm$ 0.6	
[S II]	6731	3.5 $\pm$ 1.7	3.1 $\pm$ 1.2	1.4 $\pm$ 0.9	...	1.2 $\pm$ 0.6	
He I	7065	...	5.4 $\pm$ 1.3	3.2 $\pm$ 1.0	...	6.1 $\pm$ 1.0	
[Ar III]	7136	...	2.0 $\pm$ 0.4	...	...	...	
$C(H\beta)^c$		0.080 $\pm$ 0.053	0.195 $\pm$ 0.047	0.135 $\pm$ 0.045	0.070 $\pm$ 0.054	0.180 $\pm$ 0.047	
EW(H $\beta$ ) <sup>d</sup>		156 $\pm$ 10	339 $\pm$ 34	331 $\pm$ 30	134 $\pm$ 13	459 $\pm$ 46	
EW([O III] $\lambda$ 5007) <sup>d</sup>		496 $\pm$ 19	993 $\pm$ 99	590 $\pm$ 43	726 $\pm$ 73	1019 $\pm$ 102	
EW(H $\alpha$ ) <sup>d</sup>		1073 $\pm$ 41	1950 $\pm$ 195	1787 $\pm$ 52	976 $\pm$ 98	1105 $\pm$ 111	
$F(H\beta)^e$		7.2 $\pm$ 0.4	5.0 $\pm$ 0.3	9.8 $\pm$ 1.3	6.7 $\pm$ 0.5	16.7 $\pm$ 0.7	

<sup>a</sup> $I(\lambda)$  and  $I(H\beta)$  are emission-line fluxes, corrected for the extinction derived from the Balmer decrement of hydrogen lines.

<sup>b</sup>Clipped line.

<sup>c</sup> $C(H\beta)$  is the extinction coefficient derived from the Balmer decrement of hydrogen lines.

<sup>d</sup>Rest-frame equivalent width in Å.

<sup>e</sup> $F(H\beta)$  is the observed H $\beta$  flux density in  $10^{-16}$  erg s $^{-1}$  cm $^{-2}$ .

**Table A1.** *continued* Extinction-corrected emission-line fluxes in SDSS spectra

Line	$\lambda$	$100 \times I(\lambda)/I(\text{H}\beta)^{\text{a}}$			
		J1206+5007	J1234+3901	J1505+3721	J2229+2725
[O II]	3727	44.4± 5.0	13.1± 2.4	21.3± 2.0	5.7± 1.3
H12	3750	...	...	4.2± 1.4	4.1± 1.4
H11	3771	...	...	6.4± 1.4	4.8± 1.4
H10	3798	...	6.9± 2.0	7.5± 1.4	6.0± 1.4
H9	3836	...	7.5± 1.9	11.4± 1.6	6.9± 1.5
[Ne III]	3869	23.4± 3.9	17.4± 2.5	32.9± 2.3	22.4± 2.1
H8+He I	3889	23.8± 3.8	22.6± 2.7	24.8± 2.0	19.5± 2.0
H7+[Ne III]	3969	17.6± 3.6	23.4± 2.8	29.8± 2.1	23.4± 2.1
H $\delta$	4101	27.2± 4.0	27.7± 2.9	33.3± 2.2	26.0± 2.2
H $\gamma$	4340	46.0± 4.6	47.7± 3.6	51.2± 2.7	46.3± 2.9
[O III]	4363	11.1± 3.0	6.9± 1.8	14.7± 1.5	14.0± 1.6
He I	4471	...	3.3± 1.4	2.9± 1.0	3.9± 1.1
He II	4686	...	3.1± 1.4	4.7± 1.1	2.1± 0.8
H $\beta$	4861	100.0± 6.5	100.0± 5.1	100.0± 3.9	100.0± 4.3
[O III]	4959	82.9± 5.9	64.5± 4.0	116.8± 4.2	100.3± 4.3
[O III]	5007	250.8±10.9	185.0± 7.0	335.6± 4.7	312.3± 9.2
He I	5876	9.7± 2.3	10.0± 1.6	9.2± 1.1	9.5± 1.3
[O I]	6300	...	...	...	0.7± 0.5
[S III]	6312	...	...	...	...
H $\alpha$	6563	273.1±11.8	246.7± 9.1	272.7± 8.0	270.9± 8.8
[N II]	6583	1.6± 0.7	0.7± 0.4	1.1± 0.6	0.3± 0.2
He I	6678	...	3.7± 1.0	2.4± 0.6	2.3± 0.7
[S II]	6717	3.2± 1.5	...	...	...
[S II]	6731	3.0± 1.5	...	...	...
He I	7065	...	4.5± 1.1	4.7± 0.8	4.5± 0.9
[Ar III]	7136	...	...	1.6± 0.6	0.8± 0.5
$C(\text{H}\beta)^{\text{c}}$		0.125±0.052	0.145±0.044	0.100±0.036	0.060±0.039
EW(H $\beta$ ) <sup>d</sup>		219±15	276±15	298±30	580±48
EW([O III] $\lambda$ 5007) <sup>d</sup>		429±18	610±24	351±35	1884±24
EW(H $\alpha$ ) <sup>d</sup>		1144±50	522±19	1717±172	2543±206
$F(\text{H}\beta)^{\text{e}}$		7.4±0.5	12.4±0.7	24.7±0.9	17.8±0.7

<sup>a</sup> $I(\lambda)$  and  $I(\text{H}\beta)$  are emission-line fluxes, corrected for the extinction derived from the Balmer decrement of hydrogen lines.

<sup>b</sup>Clipped line.

<sup>c</sup> $C(\text{H}\beta)$  is the extinction coefficient derived from the Balmer decrement of hydrogen lines.

<sup>d</sup>Rest-frame equivalent width in Å.

<sup>e</sup> $F(\text{H}\beta)$  is the observed H $\beta$  flux density in  $10^{-16}$  erg s $^{-1}$  cm $^{-2}$ .

**Table A2.** Electron temperatures, electron number densities and element abundances in H II regions

Parameter	Galaxy				
	J0122+0048	J0139+1542	J0811+4730	J0837+1921	J1004+3256
$T_e$ ([O III]), K	21540±4520	23510±3480	21900±4580	25000±4100	24310±2200
$T_e$ ([O II]), K	15610±3000	15250±1950	15570±2940	14730±1900	15000±1120
$T_e$ ([S III]), K	19570±3750	20430±2890	19820±3800	20870±3400	20730±1820
$N_e$ ([S II]), cm <sup>-3</sup>	500±500	10±10	110±110	678±678	
$O^+ / H^+ \times 10^5$	0.44±0.08	0.43±0.06	0.14±0.03	0.32±0.05	0.09±0.02
$O^{2+} / H^+ \times 10^5$	1.24±0.08	1.24±0.08	0.80±0.06	1.31±0.11	1.32±0.06
$O^{3+} / H^+ \times 10^6$	...	...	...	...	0.29±0.18
$O / H \times 10^5$	1.68±0.12	1.68±0.10	0.94±0.07	1.63±0.12	1.44±0.07
12+log(O/H)	7.22±0.03	7.22±0.03	6.97±0.03	7.21±0.03	7.16±0.02
$N^+ / H^+ \times 10^7$	...	2.14±0.85	0.42±0.05	...	
ICF(N) <sup>a</sup>	...	3.81	6.25	...	
$N / H \times 10^6$	...	0.81±0.33	0.26±0.32	...	
log(N/O)	...	-1.31±0.18	-1.56±0.53	...	
$Ne^{2+} / H^+ \times 10^5$	0.24±0.05	0.27±0.03	0.15±0.03	0.29±0.04	0.26±0.02
ICF(Ne) <sup>a</sup>	1.11	1.11	1.06	1.08	1.04
$Ne / H \times 10^5$	0.27±0.05	0.30±0.04	0.16±0.03	0.31±0.04	0.27±0.02
log(Ne/O)	-0.79±0.09	-0.74±0.06	-0.77±0.09	-0.71±0.07	-0.73±0.04
$S^+ / H^+ \times 10^7$	0.69±0.22	...	...	...	...
$S^{2+} / H^+ \times 10^6$	0.15±0.36	...	...	...	...
ICF(S) <sup>a</sup>	1.16	...	...	...	...
$S / H \times 10^6$	0.25±0.42	...	...	...	...
log(S/O)	-1.82±0.73	...	...	...	...

Parameter	Galaxy			
	J1206+5007	J1234+3901	J1505+3721	J2229+2725
$T_e$ ([O III]), K	23890±4840	21210±3540	23570±1770	24260±2170
$T_e$ ([O II]), K	15140±2600	15630±2380	15240±980	15020±1120
$T_e$ ([S III]), K	20610±4010	19460±2930	20490±1470	20710±1800
$N_e$ ([S II]), cm <sup>-3</sup>	471±471	10±10	10±10	10±10
$O^+ / H^+ \times 10^5$	0.41±0.07	0.10±0.02	0.19±0.02	0.05±0.01
$O^{2+} / H^+ \times 10^5$	1.01±0.09	0.95±0.06	1.41±0.05	1.22±0.06
$O^{3+} / H^+ \times 10^6$	...	0.26±0.14	0.92±0.33	0.34±0.17
$O / H \times 10^5$	1.42±0.11	1.08±0.06	1.68±0.06	1.30±0.06
12+log(O/H)	7.15±0.04	7.03±0.02	7.23±0.02	7.11±0.02
$Ne^{2+} / H^+ \times 10^5$	0.20±0.03	0.19±0.03	0.29±0.02	0.19±0.02
ICF(Ne) <sup>a</sup>	1.12	1.05	1.07	1.03
$Ne / H \times 10^5$	0.23±0.04	0.20±0.03	0.31±0.02	0.19±0.02
log(Ne/O)	-0.80±0.08	-0.73±0.07	-0.73±0.03	-0.82±0.05
$Ar^{2+} / H^+ \times 10^7$	...	...	0.39±0.13	0.19±0.12
ICF(Ar) <sup>a</sup>	...	...	1.33	2.14
$Ar / H \times 10^7$	...	...	0.52±0.18	0.41±0.69
log(Ar/O)	...	...	-2.51±0.15	-2.50±0.73

<sup>a</sup>ICF is the ionization correction factor.